2008-07-03

Characterization of a Phased Array Feed Model

David A. Jones
Brigham Young University - Provo

CHARACTERIZATION OF A PHASED ARRAY FEED MODEL

by

David Jones

A thesis submitted to the faculty of

Brigham Young University

in partial fulfillment of the requirements for the degree of

Master of Science

Department of Electrical and Computer Engineering

Brigham Young University

August 2008

BRIGHAM YOUNG UNIVERSITY

GRADUATE COMMITTEE APPROVAL

of a thesis submitted by

David Jones

This thesis has been read by each member of the following graduate committee and by majority vote has been found to be satisfactory.

Date	Karl F. Warnick, Chair
Date	Brian D. Jeffs
Date	Michael A. Jensen

BRIGHAM YOUNG UNIVERSITY

As chair of the candidate's graduate committee, I have read the thesis of David Jones in its final form and have found that (1) its format, citations, and bibliographical style are consistent and acceptable and fulfill university and department style requirements; (2) its illustrative materials including figures, tables, and charts are in place; and (3) the final manuscript is satisfactory to the graduate committee and is ready for submission to the university library.

Date

Karl F. Warnick
Chair, Graduate Committee

Accepted for the Department

Michael J. Wirthlin
Graduate Coordinator

Accepted for the College

Alan R. Parkinson
Dean, Ira A. Fulton College of
Engineering and Technology

ABSTRACT

CHARACTERIZATION OF A PHASED ARRAY FEED MODEL

David Jones

Department of Electrical and Computer Engineering

Master of Science

Creating accurate software based models of phased array feeds (PAFs) is one of many steps to successfully integrating PAFs with current and future radio telescopes, which is a goal of many groups around the globe. This thesis characterizes the latest models of a 19 element hexagonal PAF of dipoles used by the BYU radio astronomy research group and presents comparisons of these models with experimental data obtained using a prototype array. Experiments were performed at the NRAO site in Green Bank, West Virginia, and utilized the outdoor antenna test range and 20 meter radio telescope.

Accurate modeling of the PAF requires modeling the signal and noise characteristics of the array, which is a computationally large problem. It also requires accurate modeling of the noise contribution of the receivers connected to the coupled array, which is something that has only recently been understood.

The modeled and measured element receive patterns, array impedance matrix, signal and noise correlation matrices, and efficiencies and sensitivities of the PAF are compared and promising levels of agreement are shown. Modeled sensitivity is 30 to 46% larger than measured.

ACKNOWLEDGMENTS

I would like to thank the following individuals for their assistance. Dr. Karl Warnick and Dr. Brian Jeffs for their leadership and willingness to share their talents to help me develop mine. Dr. Rick Fisher and Roger Norrod from the NRAO for their assistance in performing many of the experiments mentioned in this work. My friends and colleagues at BYU who have made my experience here enjoyable and fruitful. And lastly, my wife Amanda and my sons Clark and Parker for their patience, encouragement, and good humor.

Table of Contents

List of Tables

List of Figures

Chapter 1

Introduction

1.1 Radio Astronomy

The goal of radio astronomy is to further study, explore, and understand the universe by measuring radio waves that originate from outer space. Antennas, electronic amplifiers, and related electronic equipment are the tools used to measure radio waves. Physics, optical astronomy, and signal processing provide the tools required to extract useful information from measurements. Antennas, amplifiers, and signal processing are the subject of this work.

1.2 Advancements in Radio Astronomy

Since the first discoveries in the 1930's by Karl Jansky and Grote Reber, radio astronomy has contributed much to our knowledge of the universe [1], [2]. Many technological advancements have been and continue to be made in antenna design, amplifier design, and signal processing, among other areas. Large reflector antennas [3], [4] and arrays of reflector antennas [5], [6] have been two of the primary instruments of radio astronomy. Other advancements have included low noise wideband amplifiers [7] and wideband reflector feed antennas [8]. Signal processing for radio astronomy has grown from simple detection techniques required for single antenna radio telescopes to sophisticated synthesis imaging for arrays of telescopes. Recently, interest has been growing in the development of phased array feeds (PAFs) which is introducing challenges previously not dealt with in antenna design, amplifier design, and signal processing for radio astronomy. A feed is the antenna located at the focal point of a reflector antenna, and a phased array feed is an array of antennas that act as a feed and whose outputs are combined using a beamformer.

1.3 Current PAF Research

Phased array feeds of electrically small antenna elements will potentially provide several benefits over reflector feeds currently in use, including interference cancellation, increased sensitivity, and beam steering over a continuous region of sky. Beam steering increases both the field of view and the survey speed of a radio telescope. Array feeds for radio astronomy that are currently in use consist of electrically large elements that are usually not phased, in other words the antennas are processed as individual elements [9].

Despite the fact that phased array feeds have been in use for communications applications for several years [10], [11] several challenges remain with implementing them for radio astronomy. These challenges include requirements for gain stability, calibration, large bandwidth, and mutual coupling between closely spaced elements, which introduces deviations from expected performance of the antenna and receiver if not accounted for [12], [13], [14].

Several groups have made and are continuing to make significant steps towards simulating, understanding, building, and testing PAFs. The National Radio Astronomy Observatory (NRAO) built a 19 element array of sinuous antennas as an early demonstration of a PAF [15]. The Australian Commonwealth Scientific and Industrial Research Organization (CSIRO) is developing a PAF for use in the Australian Square Kilometer Array Pathfinder (ASKAP) [16]. The Netherlands Foundation for Research in Astronomy (ASTRON) has made progress on a wideband, dual polarized array of Vivaldi antennas [17]. The Canadian National Research Council is also developing a Vivaldi array as a phased array feed demonstrator (PHAD) [18].

Brigham Young University and the NRAO have jointly developed prototype seven and 19 element hexagonal phased array feeds consisting of dipole antennas. Initial simulation results are presented in [19], and initial measurements using the seven element array on a three meter reflector are presented in [20]. The 19 element prototype PAF was built and initial measurements were performed on the NRAO 20 meter parabolic reflector at Green Bank, West Virginia in 2007.

1.4 Thesis Contributions

The purpose of this thesis is to present simulation results for the 19 element hexagonal dipole PAF and to compare the simulations with experimental measurements. The comparisons show a previously unachieved level of agreement between the model and experimental data. Simulation results are obtained using a finite element method (FEM) numerical simulation software package to model the antenna self and mutual impedances and radiation patterns of the elements in the array without the reflector present. The results also include simulated efficiencies, signal to noise ratio, and sensitivity of the phased array feed mounted on the 20 meter reflector. An analytical antenna model similar to the one used in [19] is also studied to quantify the improvements gained by using the FEM model. Use of the FEM model and the level of achieved agreement between a PAF model and experimental results are significant improvements over previously reported results.

Another significant improvement is in the receiver noise model. Previously the noise model assumed the noise introduced by the receivers was spatially uncorrelated. The results presented in this work take into account the correlation of the receiver noise caused by the coupled array [14], [12], [13], [21]. This correlation causes an increase in the beam dependent equivalent noise temperature of the receiver.

Chapter 2

Electromagnetic and Signal Processing Background for Modeling Phased Array Feeds

This chapter presents an overview of an electromagnetic and signal processing framework for modeling signals obtained with a phased array receive antenna, with particular attention to phased arrays located near the focal plane of a reflector antenna (phased array feed, or PAF). As mentioned in the introduction, phased array feeds have applications in digital communications and in radio astronomy. Many topics discussed in this section apply equally well to both applications.

A general phased array system consisting of N antenna elements has N output signals. The array observes the signal of interest, interfering signals, and sources of noise such as thermal noise. The signals and noise are spatially sampled by the antennas which produces a voltage across the terminals of each antenna. Each antenna terminal is loaded by a receiver which contains amplifiers, transmission lines, filters, mixers, and an A/D converter, etc. The antennas introduce thermal noise because of their ohmic resistance. Receivers also introduce thermal, flicker, and shot noise to the signal. The outputs of the array are the voltages measured at the A/D outputs. In the following signal processing stages a complex baseband, or phasor, representation for the signals and noise is used and the channel gains due to the amplifiers are normalized to unity.

A characteristic of phased arrays is the way in which the output signals are combined. Each voltage is shifted in phase and/or scaled in amplitude and the resulting voltages are summed to produce a single beamformed output as seen in Figure 2.1. This phase shift and amplitude scaling can be represented as a multiplication by a complex weight w_m^*, where $(\cdot)^*$ represents complex conjugation. As will be shown

in Sections 2.1–2.6, the spatial correlation matrix of the loaded output voltages is a helpful tool in modeling the phased array feed and processing the received voltages.

The voltages on the N channels and the complex weights can be represented as N element column vectors $\mathbf{v}$ and $\mathbf{w}$ respectively. Using this notation the beamformer output voltage is

$$y = \mathbf{w}^H \mathbf{v}, \tag{2.1}$$

where $(\cdot)^H$ represents a conjugate transpose.

A common receiver design technique is to place low noise amplifiers (LNAs) as close to the antennas as possible, which lessens the significance of the noise contributed by the rest of the receiver because amplifiers typically have high gain in the forward direction. They also have high isolation in the reverse direction. Unless otherwise stated it will be assumed that LNAs are placed immediately following the antennas and that they provide ideal isolation in the reverse direction.

The output voltage $\mathbf{v}$ referred to the input of the LNAs is given by

$$\mathbf{v} = \underbrace{\mathbf{v}_s}_{\text{signal of interest}} + \underbrace{\mathbf{v}_t + \mathbf{v}_{loss} + \mathbf{v}_{lna} + \mathbf{v}_{rec2}}_{\text{noise}} + \underbrace{\sum_{u=1}^{U} \mathbf{v}_{i,u}}_{\text{interferers}}, \tag{2.2}$$

where $\mathbf{v}_s$ is the voltage due to the signal of interest, $\mathbf{v}_{i,u}$ is the voltage due to the u^{th} interferer, $\mathbf{v}_t$ is the voltage due to the thermal noise caused by the environment surrounding the PAF, $\mathbf{v}_{loss}$ is the voltage due to the thermal noise caused by the ohmic resistance of the antennas, $\mathbf{v}_{lna}$ is the noise voltage caused by the LNAs, and $\mathbf{v}_{rec2}$ is the noise voltage caused by the rest of the receiver. Unless otherwise stated we assume $U = 1$ and $\mathbf{v}_{i,1} = \mathbf{v}_i$. The simplified system model is illustrated in Figure 2.1.

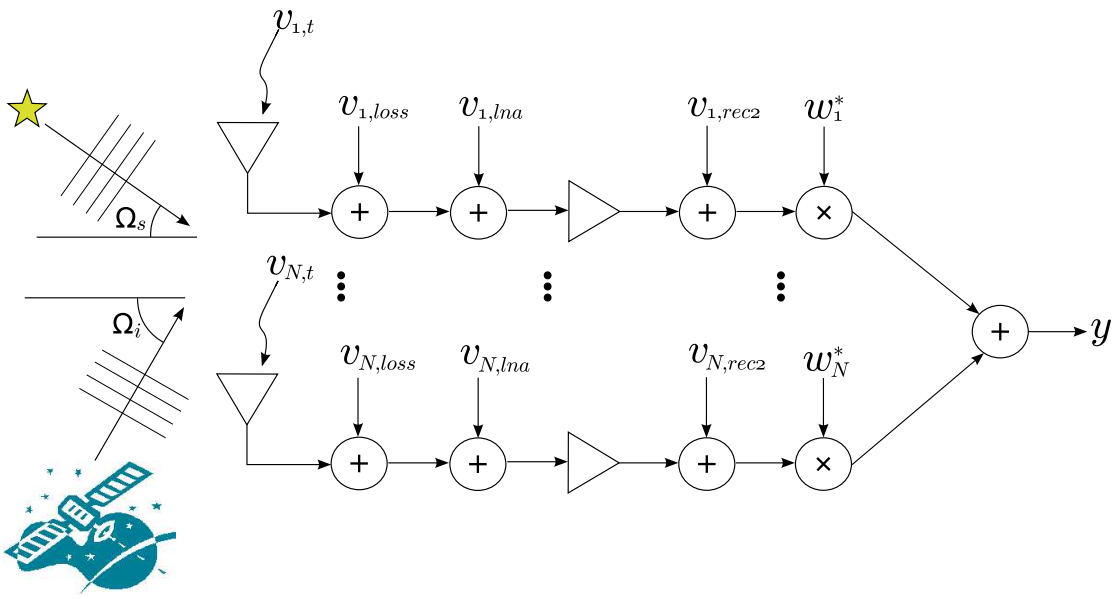

Figure 2.1: System block diagram. The voltages v_{lna}, v_{loss}, and v_{rec2} represent noise added to the signal after spatial sampling by the antennas. The voltage v_t and the interfering signal with incident angle Ω_i represent noise added to the signal before spatial sampling.

The spatial correlation matrix of the output voltages is given by

$$\begin{aligned}
\mathbf{R}_v &= \mathrm{E}\left[\mathbf{v}\mathbf{v}^H\right] \\
&= \mathrm{E}\left[\mathbf{v}_s\mathbf{v}_s^H\right] + \mathrm{E}\left[\mathbf{v}_i\mathbf{v}_i^H\right] + \mathrm{E}\left[\mathbf{v}_t\mathbf{v}_t^H\right] + \mathrm{E}\left[\mathbf{v}_{loss}\mathbf{v}_{loss}^H\right] + \dots \\
&\quad \mathrm{E}\left[\mathbf{v}_{lna}\mathbf{v}_{lna}^H\right] + \mathrm{E}\left[\mathbf{v}_{rec2}\mathbf{v}_{rec2}^H\right] \\
&= \mathbf{R}_s + \mathbf{R}_i + \mathbf{R}_t + \mathbf{R}_{loss} + \mathbf{R}_{lna} + \mathbf{R}_{rec2} \\
&= \mathbf{R}_s + \mathbf{R}_n,
\end{aligned} \tag{2.3}$$

where $\mathrm{E}[\cdot]$ denotes expectation and $\mathbf{R}_n$ is the noise correlation matrix.

In practice the correlation matrices must be estimated from discrete time samples of the output voltages, denoted $\mathbf{v}[n]$. The correlation matrix is estimated by assuming stationarity and averaging correlation matrices over several time samples,

$$\mathbf{R}_v = \lim_{T\to\infty} \frac{1}{T} \sum_{n=1}^{T} \mathbf{v}[n]\mathbf{v}^H[n]. \tag{2.4}$$

Sections 2.1–2.6 discuss how the correlation matrices in Equation (2.3) may be computed for use in a software based model of a phased array feed. The development given in these sections is available in the literature [22], [23], [24] with some changes in notation. It is included here for reference.

2.1 Signal Model

In this section we discuss a method for obtaining the open circuit voltages at the antenna terminals due to an incident plane wave emanating from a point source, transforming the open circuit voltages to voltages across a load, and calculating the correlation matrix $\mathbf{R}_s$. A similar development can be used to find $\mathbf{R}_i$.

Using the reciprocity theorem of electromagnetics it is possible to express the open circuit voltage at a receiving antenna's terminals in terms of the far electric field radiated by the antenna if it was a transmitting antenna [25]. Since the electric field is a function of angle, the open circuit voltages are also a function of the direction of propagation, or angle, of the incident plane wave with respect to the antenna. This angle is denoted Ω in Figure 2.1 and is shorthand for the elevation and azimuth angles, θ and ϕ respectively. The open circuit voltage also depends on the distance from the source to the array, but amplitude changes due to propagation loss are included in the amplitude term of the incident plane wave. The expression for the open circuit voltage across the nth antenna's terminals is

$$\begin{aligned} \check{v}_n(\theta,\phi) &= \frac{4\pi j r e^{jkr}}{k\eta I_0}(\hat{p}E^{sig}) \cdot \overline{E}_n(r,\theta,\phi) \\ &= \frac{4\pi j r e^{jkr}}{k\eta I_0}E^{sig}(\hat{p} \cdot \overline{E}_n(\overline{r})), \end{aligned} \tag{2.5}$$

where j is the imaginary number, k is the wave number of the signal, η is the characteristic impedance of free space, r is an arbitrary, normalized distance, I_0 is the input current at the feed of the antenna used to calculate the open circuit radiation pattern, $\overline{E}_n(r,\theta,\phi)$, and $\hat{p}$ and E^{sig} are the polarization and amplitude of the incident plane wave respectively.

The vector of open circuit voltages, $\check{\mathbf{v}} = [\check{v}_1, \ldots, \check{v}_N]^T$ can be converted to voltages across a load by using a multiport network version of voltage division,

$$\mathbf{v}(\theta, \phi) = \mathbf{Q}\check{\mathbf{v}}(\theta, \phi), \tag{2.6}$$

$$\mathbf{Q} = \mathbf{Z}_L(\mathbf{Z}_A + \mathbf{Z}_L)^{-1}, \tag{2.7}$$

where $\mathbf{Z}_L$ is a diagonal matrix where the diagonal elements are the driving point impedances of the LNAs and $\mathbf{Z}_A$ is the impedance matrix representing the input impedance of the array. The diagonal elements of $\mathbf{Z}_A$ represent the self impedances of the antenna elements, and the off-diagonal elements represents the mutual impedances between antenna elements.

Combining Equations (2.5), (2.6), and (2.3) and assuming the signal is coherent and stationary the signal correlation matrix is

$$\mathbf{R}_s = \mathbf{Q}\check{\mathbf{R}}_s\mathbf{Q}^H, \tag{2.8}$$

where $\check{\mathbf{R}}_s$ is the correlation matrix of the open circuit voltages whose elements are obtained from Equation (2.5) and are given by

$$\check{R}_{s,mn} = \frac{16r^2\lambda^2}{|I_0|^2}\frac{|E^{sig}|^2}{2\eta}\frac{1}{2\eta}\mathrm{E}\left[(\hat{p}\cdot\overline{E}_m(\overline{r}))(\hat{p}\cdot\overline{E}_n(\overline{r}))^*\right], \tag{2.9}$$

where λ is the wavelength of the signal and the expectation is over time to include the effect of a randomly polarized signal. Defining $\mathbf{a}_p = [a_{p,1}, \ldots, a_{p,N}]^T$ to be the array response vector for a particular polarization, where $a_{p,m}(\overline{r}) = \hat{p}\cdot\overline{E}_m(\overline{r})$, Equation (2.8) can be written as

$$\begin{aligned}\mathbf{R}_s &= \frac{16r^2\lambda^2}{|I_0|^2}S^{sig}\mathbf{Q}\mathrm{E}\left[\frac{1}{2\eta}\mathbf{a}_p(\overline{r})\mathbf{a}_p^H(\overline{r})\right]\mathbf{Q}^H \\ &= \frac{16r^2\lambda^2}{|I_0|^2}S^{sig}\mathbf{Q}\mathrm{E}\left[\mathbf{B}_p(\overline{r})\right]\mathbf{Q}^H,\end{aligned} \tag{2.10}$$

where $\mathbf{B}_p = \mathbf{a}_p \mathbf{a}_p^H/(2\eta)$ is the array response matrix for a particular polarization, and $S^{sig} = |E^{sig}|^2/(2\eta)$ is the incident flux density. If the polarization is random, a common assumption in radio astronomy, the expectation in Equation (2.10) introduces a factor of one half. If all the elements have far field patterns that are polarized in the same direction the correlation matrix becomes

$$\begin{aligned} \mathbf{R}_s &= \frac{16r^2\lambda^2}{|I_0|^2}\frac{S^{sig}}{2}(\mathbf{B}_{co}(\overline{r}) + \mathbf{B}_{cross}(\overline{r})) \\ &= \frac{16r^2\lambda^2}{|I_0|^2}S^{sig,p}(\mathbf{B}_{co}(\overline{r}) + \mathbf{B}_{cross}(\overline{r})), \end{aligned} \tag{2.11}$$

where $\mathbf{B}_{co}$ and $\mathbf{B}_{cross}$ are the array response matrices for the co-polarized and cross-polarized incident fields respectively. The factor of $S^{sig}/2 = S^{sig,p}$ is the incident power in a single polarization.

From Equations (2.8)–(2.11) it is seen that one must know the far field pattern of each element in an array, $\overline{E}_m(\overline{r})$, to correctly model $\mathbf{R}_s$ as a function of incident angle. For a PAF, which is mounted near the focal plane of a reflector antenna, the far field pattern of an element in the array can be estimated using the physical optics (PO) approximation, which provides a simple relationship between the field pattern incident on the reflector and the surface current on the reflector

$$\overline{J}_{s,m}(\overline{r}_d) = 2\hat{n}_d \times \overline{H}^i_m(\overline{r}_d), \tag{2.12}$$

where $\overline{J}_{s,m}(\overline{r}_d)$ is the surface current on the reflector due to the mth element, $\hat{n}_d$ is the unit normal to the surface of the reflector, $\overline{H}^i_m(\overline{r}_d)$ is the *bare array* magnetic field radiated by the mth element evaluated on the surface of the reflector, in other words it is the magnetic field that would be radiated by the array if no reflector were present, and $\overline{r}_d$ represents a point on the surface of the reflector. The total far electric field $\overline{E}_m(\overline{r})$ is then found by putting the surface current in the free space far field

radiation integral and adding it to the bare array electric field,

$$\begin{aligned}\overline{E}_m(\overline{r}) &= \overline{E}^i_m(\overline{r}) + \overline{E}^r_m(\overline{r}) \\ &= \overline{E}^i_m(\overline{r}) - jk\eta\frac{e^{-jkr}}{4\pi r}(1-\hat{r}\hat{r}\cdot)\int e^{jk\hat{r}\cdot\overline{r}_d}J_{s,m}(\overline{r}_d)d\overline{r}_d,\end{aligned} \tag{2.13}$$

where $\overline{E}^r_m(\overline{r})$ is the reflected far field.

The computational load required to perform the integration in Equation (2.13) can be a significant hurdle for large reflectors because the surface current is highly oscillatory; therefore various approximations can be made to simplify the integration. The PO approximation ignores blockage by the feed and support struts and edge diffraction by the edge of the reflector.

If the source is a radio astronomical signal of interest the signal flux density S^{sig}, which has units W/m^2, is often expressed in terms of F^{sig} which is the signal flux density in units of Janskys. The conversion from Janskys to W/m^2 is

$$S^{sig} = F^{sig}B_n 10^{-26}, \tag{2.14}$$

where B_n is the noise equivalent bandwidth of the receiver system.

For the remainder of this thesis it is assumed that the array feed receives only a single polarization and that the polarization of the signal of interest is random, therefore the incident flux density in a single polarization, $S^{sig,p}$ and $F^{sig,p} = F^{sig}/2$, will be used unless otherwise stated.

2.1.1 Physical Optics Approximations

This section describes two methods used to compute the far field radiation pattern of the mth element $\overline{E}_m(\overline{r})$ using Equation (2.13).

The first method, described in [26], converts the two dimensional integration into a one dimensional integration. This method assumes a form for the radiation pattern of a feed element. If we let $\overline{r}_d = (r_d, \theta_d, \phi_d)$ be a point on the reflector and if we let r'_d be the distance from the mth feed element to the point on the reflector

then the assumed form is

$$\overline{E}_m^i(\overline{r}_d) = \frac{e^{-jkr'_d}}{r'_d}(\hat{\theta}E_P(\theta_d)\sin(\phi_d) - \hat{\phi}H_P(\theta_d)\cos(\phi_d)), \tag{2.15}$$

where E_P and H_P are the E and H-plane radiation patterns respectively. This method assumes that θ is small. Figure 2.2, which is a comparison between this method and the second, more accurate method, shows that as θ increases the magnitude does not deviate from the more accurate method, but the phase deviation increases.

The second method used to integrate Equation (2.13) is a two dimensional midpoint quadrature rule. This method is rather brute force and requires more computing resources, however, it is more accurate than the one dimensional integration method. Other methods for doing this integration are available in the literature [27].

The scattering and blockage by the feed and the feed support struts is also ignored in the model.

2.2 Thermal Noise Model

The correlation matrices due to external thermal noise and to the ohmic resistance of the antennas are discussed in this section. In this development it is useful to define a matrix that characterizes the total radiated power of the array as a transmitter. We will call this the overlap matrix, $\mathbf{A}$, with elements defined by

$$A_{m,n} = \frac{1}{2\eta}\int_\Omega \overline{E}_m(\overline{r}) \cdot \overline{E}_n^*(\overline{r}) r^2 d\Omega, \tag{2.16}$$

where $d\Omega = \sin(\theta)d\theta d\phi$ and the region of integration is a closed surface, usually a sphere, surrounding the array. It can be shown that the total radiated power by an array is

$$P_{rad} = \frac{1}{|I_0|^2}\mathbf{i}^T\mathbf{A}\mathbf{i}^*, \tag{2.17}$$

where $\mathbf{i}$ is a vector of input currents for the transmitting array. Since the overlap matrix is related to the total radiated power it is possible to use the bare array electric fields, $\overline{E}_m^i(\overline{r})$, instead of the electric fields due to the reflector and the array,

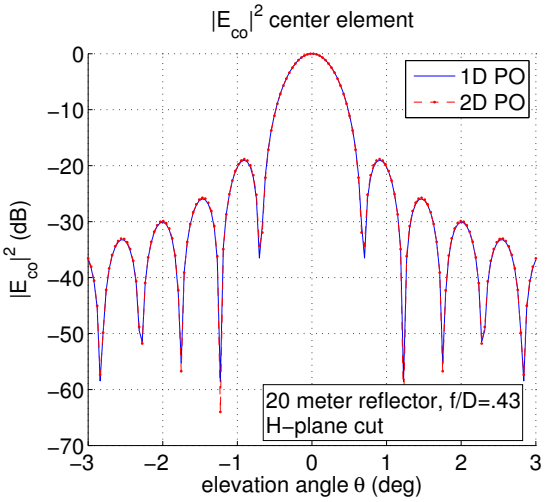

(a) Magnitude, center element.

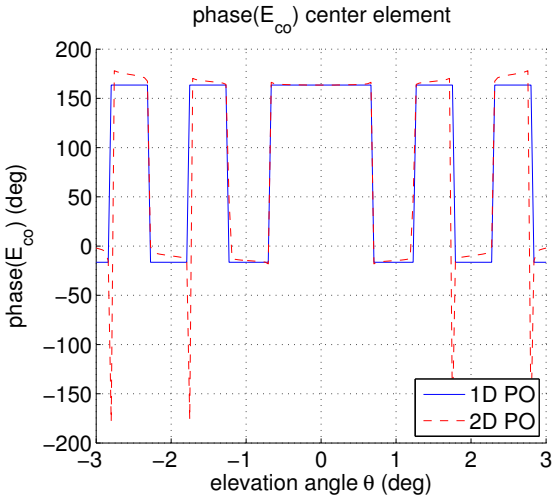

(b) Phase, center element.

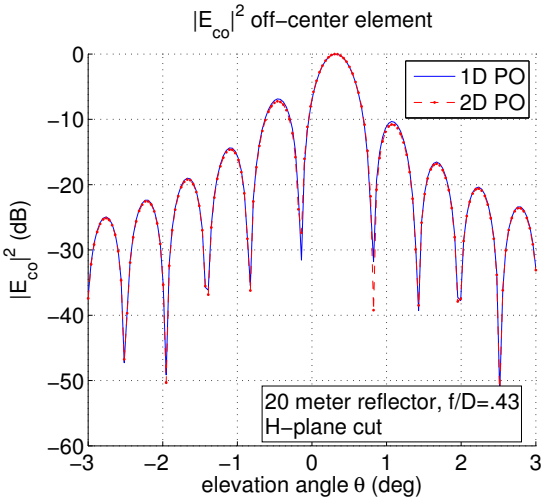

(c) Magnitude, off-center element.

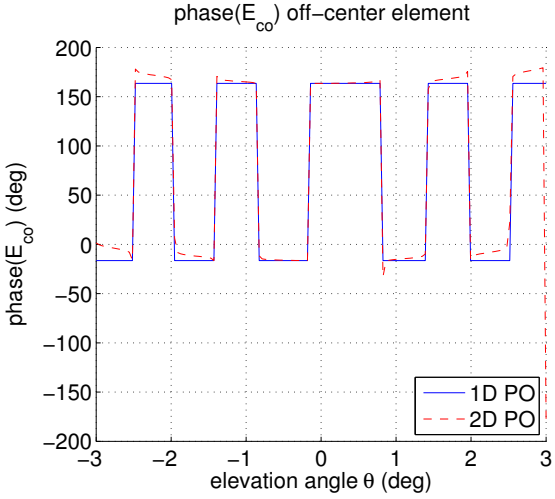

(d) Phase, off-center element.

Figure 2.2: Comparing the co-polarization component of the far electric field of two elements in the 19 element array located on the focal plane of a 20 meter parabolic reflector with $f/D = .43$ using both the one and two dimensional physical optics methods. (a): magnitude, center element. (b): phase, center element. (d): magnitude, off-center element. (d): phase, off-center element. The analytical dipole model was used.

$\overline{E}_m(\overline{r})$, in Equation (2.16). This is attractive since it is usually requires much less computation to integrate the bare array fields. It can also be shown that the total input power to a transmitting array is

$$P_{in} = \frac{1}{2}\mathbf{i}^T\mathbf{R}_A\mathbf{i}^*, \tag{2.18}$$

where $\mathbf{R}_A = \mathrm{Re}\,(\mathbf{Z}_\mathrm{A})$. The power dissipated in the antenna is the difference between the input and radiated powers

$$P_{loss} = \frac{1}{2}\mathbf{i}^T\underbrace{(\mathbf{R}_A - \frac{2}{|I_0|^2}\mathbf{A})}_{\mathbf{R}_{A,ohmic}}\mathbf{i}^*. \tag{2.19}$$

From this it can be seen that $\mathbf{R}_{A,ohmic}$ is the ohmic portion of the array mutual resistance matrix, $\mathbf{R}_A$, and that $\frac{2}{|I_0|^2}\mathbf{A}$ is the radiation portion.

From the results in [22] it can be shown that the correlation matrix of open circuit voltages due to thermal noise generated by blackbody radiation from the array's surroundings with brightness temperature distribution $T_B(\Omega)$ have elements that are given by

$$\check{R}_{t,mn} = \frac{16}{|I_0|^2}k_b B_n \frac{1}{2\eta}\int_\Omega T_B(\Omega)\overline{E}_m(\overline{r})\cdot\overline{E}_n^*(\overline{r})r^2 d\Omega, \tag{2.20}$$

where k_b is Boltzmann's constant. The correlation matrix of loaded voltages, $\mathbf{R}_t$, is related to $\check{\mathbf{R}}_t$ in the same way that $\mathbf{R}_s$ and $\check{\mathbf{R}}_s$ are related in Equation (2.8). If $T_B(\Omega) = T_{iso}$ is a constant over all Ω then we say that the thermal noise is spatially isotropic and using Equation (2.16), Equation (2.20) becomes

$$\mathbf{R}_t = \mathbf{R}_{iso} = \frac{16}{|I_0|^2}k_b T_{iso} B_n \mathbf{Q}\mathbf{A}\mathbf{Q}^H \quad \text{if } T_B(\Omega) = T_{iso}. \tag{2.21}$$

Even though the actual thermal noise environment may not be isotropic, $\mathbf{R}_{iso}$ still plays an important role in defining antenna efficiencies, as shown in Section 2.5.

If the actual brightness temperature distribution can be separated into a sky temperature T_{sky} and a ground temperature T_g, the integral in Equation (2.20) can

be separated into one integral over the sky region and another over the ground region. If a reflector antenna is used the integral over the ground region can be approximated by integrating the bare array electric fields over the region that extends from the edge of the reflector to the edge of the ground region, which is the horizontal plane if the reflector is pointed towards zenith; this region is typically called the spillover region because the bare array receive pattern, which is designed to accept power in the direction of the reflector, cannot be completely contained to the reflector. Spillover noise is a major contributor to the overall system noise because the ground temperature is on the order of 300 K whereas the sky temperature is on the order of 3 K at L band frequencies. We will define the thermal noise correlation matrix due to thermal noise in the spillover region to be

$$\mathbf{R}_{sp} = \frac{16}{|I_0|^2} k_b T_g B_n \mathbf{Q} \mathbf{A}_{sp} \mathbf{Q}^H, \tag{2.22}$$

where $\mathbf{A}_{sp}$ can be approximated by

$$A_{sp,mn} = \frac{1}{2\eta} \int_{\Omega_{sp}} \overline{E}_m^i(\overline{r}) \cdot \overline{E}_n^{i*}(\overline{r}) r^2 d\Omega, \tag{2.23}$$

A close approximation to the thermal noise correlation matrix that is actually realized by a PAF is

$$\mathbf{R}_t \approx \mathbf{R}_{sp} \quad \text{if the reflector is pointed towards zenith and } T_g \gg T_{sky}. \tag{2.24}$$

Lossy antenna elements will also generate thermal noise which can also be understood in terms of a correlation matrix. From the results in [28] it can be shown that if the array is in thermal equilibrium with a spatially isotropic thermal noise environment the thermal noise correlation matrix due to the external and internal

thermal noise is

$$\mathbf{R}_t + \mathbf{R}_{loss} = \mathbf{R}_{te} = 8k_b T_{iso} B_n \mathbf{Q}\mathbf{R}_A\mathbf{Q}^H \quad \text{if } T_B(\Omega) = T_{iso} \text{ and } T_a = T_{iso}, \tag{2.25}$$

where T_a is the physical temperature of the antenna and it was assumed that $\mathbf{Z}_A + \mathbf{Z}_A^H = \mathbf{R}_A$. The correlation matrix $\mathbf{R}_{te}$ plays a role similar to $\mathbf{R}_{iso}$ in that even though $T_B(\Omega) \neq T_{iso}$ and $T_a \neq T_{iso}$ in practice, $\mathbf{R}_{te}$ is used to define antenna efficiencies and available power at the output of the beamformer, see Sections 2.4 and 2.5.

In Equation (2.25) $\mathbf{R}_t$ can be replaced with $\mathbf{R}_{iso}$ because $T_B(\Omega) = T_{iso}$. Rearranging the equation to solve for $\mathbf{R}_{loss}$ results in

$$\mathbf{R}_{loss} = \mathbf{R}_{te} - \mathbf{R}_{iso} \quad \text{if } T_a = T_{iso}. \tag{2.26}$$

Using Equations (2.19) and (2.21) $\mathbf{R}_{te} - \mathbf{R}_{iso}$ is found to be

$$\mathbf{R}_{loss} = \mathbf{R}_{te} - \mathbf{R}_{iso} = 8k_b T_{iso} B_n \mathbf{Q}\mathbf{R}_{A,ohmic}\mathbf{Q}^H \quad \text{if } T_a = T_{iso}. \tag{2.27}$$

If the array is not in thermal equilibrium with its environment T_{iso} in Equation (2.27) is replaced by the physical temperature of the antenna, T_a. The correlation matrix due to antenna ohmic resistance is then

$$\mathbf{R}_{loss} = 8k_b T_a B_n \mathbf{Q}\mathbf{R}_{A,ohmic}\mathbf{Q}^H. \tag{2.28}$$

Comparing Equations (2.17)–(2.19), (2.21), (2.25), and (2.28), it can be seen that the relationship between P_{rad} and $\mathbf{R}_{iso}$ is similar to the relationship between P_{in} and $\mathbf{R}_{te}$ and the relationship between P_{loss} and $\mathbf{R}_{loss}$.

2.3 Receiver Noise Model

The correlation matrix due to receiver noise is

$$\mathbf{R}_{rec} = \mathbf{R}_{lna} + \mathbf{R}_{rec2}. \tag{2.29}$$

In many cases the gain of the LNAs is large enough that the correlation matrix due to noise introduced by the rest of the receiver following the LNAs, R_{rec2}, can be ignored. An expression for R_{lna} is given below.

The LNA noise model assumed is shown in Figures 2.3 and 2.4. The noise contribution from the LNAs is assumed to consist of partially correlated noise and current sources, $\mathbf{v}_{n,R}$ and $\mathbf{i}_{n,R}$ respectively. The noise sources have RMS densities $\bar{\mathbf{v}}_{n,R}$ and $\bar{\mathbf{i}}_{n,R}$ which have units of $V/\sqrt{Hz}$ and $A/\sqrt{Hz}$ respectively. The noise sources correlated according to

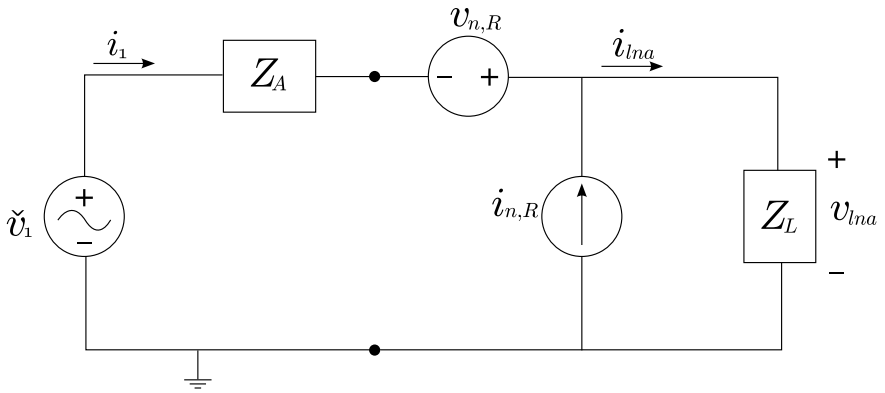

Figure 2.3: Idealized equivalent circuit of a single noisy LNA connected to an antenna represented by a Thévenin equivalent open circuit voltage $\check{v}_1$ and Thévenin impedance Z_A.

$$\mathbf{i}_{n,R} = \mathbf{Y}_c \mathbf{v}_{n,R} + \mathbf{i}_{u,R}, \tag{2.30}$$

where $\mathbf{Y}_c$ is a diagonal matrix consisting of correlation admittances for each LNA along the diagonal and $\mathbf{i}_{u,R}$ is uncorrelated with $\mathbf{v}_{n,R}$.

From Equation (2.3) we have

$$\mathbf{R}_{lna} = \mathrm{E}\left[\mathbf{v}_{lna}\mathbf{v}_{lna}^H\right]. \tag{2.31}$$

Using network circuit theory, the circuit diagram in Figure 2.4, and by setting the

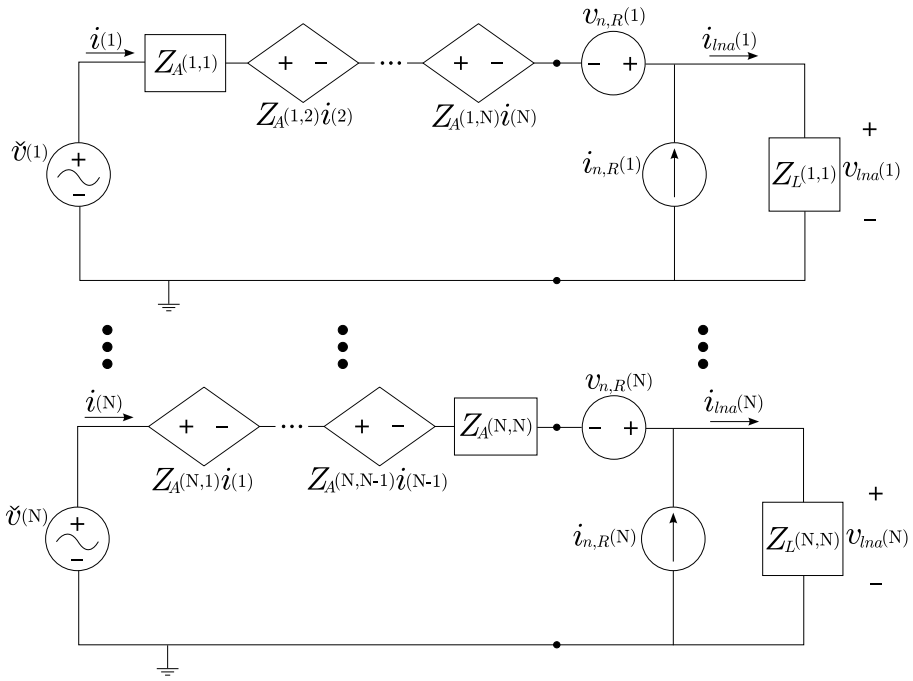

Figure 2.4: Idealized equivalent circuit of N noisy LNAs connected to an antenna array represented by a Thévenin equivalent open circuit voltage $\check{\mathbf{v}}$ and Thévenin impedance $\mathbf{Z}_A$. Array notation is used for indexing the elements of the vectors and matrices, ie. $\mathbf{Z}_A(m,n) = \mathbf{Z}_{A,mn}$.

Thévenin equivalent open circuit voltages, $\check{\mathbf{v}}$, equal to zero $\mathbf{R}_{lna}$ can be expressed as

$$\begin{aligned}\mathbf{R}_{lna} = \mathbf{Q}\big(&\mathbf{Z}_A \mathrm{E}\left[\mathbf{i}_{n,R}\mathbf{i}_{n,R}^H\right]\mathbf{Z}_A^H + \mathbf{Z}_A \mathrm{E}\left[\mathbf{i}_{n,R}\mathbf{v}_{n,R}^H\right] + \mathrm{E}\left[\mathbf{v}_{n,R}\mathbf{i}_{n,R}^H\right]\mathbf{Z}_A^H + \dots \\ &\mathrm{E}\left[\mathbf{v}_{n,R}\mathbf{v}_{n,R}^H\right]\big)\mathbf{Q}^H.\end{aligned} \tag{2.32}$$

By definition of the RMS densities

$$\begin{aligned}\mathrm{E}\left[\mathbf{i}_{n,R}\mathbf{i}_{n,R}^H\right] &= 2B_n\bar{\mathbf{I}}_{n,R}^2, \\ \mathrm{E}\left[\mathbf{v}_{n,R}\mathbf{v}_{n,R}^H\right] &= 2B_n\bar{\mathbf{V}}_{n,R}^2,\end{aligned} \tag{2.33}$$

where $\bar{\mathbf{I}}_{n,R} = \mathrm{diag}(\bar{\mathbf{i}}_{n,R})$, $\bar{\mathbf{V}}_{n,R} = \mathrm{diag}(\bar{\mathbf{v}}_{n,R})$, and $\mathrm{diag}(\cdot)$ is an operator that converts a vector to a diagonal matrix and vice versa. Combining Equations (2.30) and (2.32)

and using the fact that $\mathbf{i}_{u,R}$ and $\mathbf{v}_{n,R}$ are uncorrelated Equation (2.32) becomes

$$\mathbf{R}_{lna} = 2B_n\mathbf{Q}(\bar{\mathbf{V}}^2_{n,R} + \mathbf{Z}_A\mathbf{Y}_c\bar{\mathbf{V}}^2_{n,R} + \bar{\mathbf{V}}^2_{n,R}\mathbf{Y}^H_c\mathbf{Z}^H_A + \mathbf{Z}_A\bar{\mathbf{I}}^2_{n,R}\mathbf{Z}^H_A)\mathbf{Q}^H. \tag{2.34}$$

For a single LNA the parameters $\bar{v}_{n,R}$, $\bar{i}_{n,R}$, and Y_c describe its noise characteristics. These parameters can also be written in terms of the minimum possible equivalent noise temperature T_{min}, the source admittance which minimizes in the equivalent noise temperature, Y_{opt}, and the equivalent noise resistance R_N. For two or more LNAs these parameters can be expressed as diagonal matrices with each diagonal element corresponding to a separate LNA. These parameters are related to the RMS voltage and current densities and the correlation admittance according to

$$\begin{aligned}
\mathbf{Y}_c &= \frac{1}{2T_0}\mathbf{T}_{min}\mathbf{R}_N^{-1} - \mathbf{Y}_{opt}, \\
\bar{\mathbf{I}}^2_{n,R} &= \mathbf{Y}_{opt}\mathbf{Y}^H_{opt}\bar{\mathbf{V}}^2_{n,R}, \\
\bar{\mathbf{V}}^2_{n,R} &= 4k_bT_0\mathbf{R}_N,
\end{aligned} \tag{2.35}$$

where $T_0 = 290K$. Using these relationships Equation (2.34) becomes

$$\begin{aligned}
\mathbf{R}_{lna} = 8k_bT_0B_n\mathbf{Q}\Big(&\frac{1}{2T_0}(\mathbf{Z}_A\mathbf{T}_{min} + \mathbf{T}_{min}\mathbf{Z}^H_A) + \ldots \\
&\mathbf{Z}_A(\mathbf{Y}_A - \mathbf{Y}_{opt})\mathbf{R}_N(\mathbf{Y}_A - \mathbf{Y}_{opt})^H\mathbf{Z}^H_A\Big)\mathbf{Q}^H.
\end{aligned} \tag{2.36}$$

2.4 Available Power and Equivalent Temperature

It is often convenient to express beamformer outputs in terms of either available power at the antenna terminals or an equivalent temperature. This section will discuss how these two quantities are obtained.

For a single antenna the available power across a load is calculated by setting the load impedance equal to the conjugate of the antenna impedance, $Z_L = Z^*_A$. For a beamformer, however, the output voltages are summed and the power is calculated across a single load, which makes it impossible to set the load impedance (a scalar)

equal to the conjugate of the antenna impedance (a matrix). One way to think of this is that since the scaling of the weights, $\mathbf{w}$, is arbitrary the output power is arbitrary, all that can be said is that the available power, $P_{v,av}$, is proportional to the actual power $P_{v,actual}$, so that

$$P_{v,actual} = \frac{\mathrm{E}\left[yy^*\right]}{2R_L} \tag{2.37}$$

$$= \frac{\mathbf{w}^H \mathrm{E}\left[\mathbf{v}\mathbf{v}^H\right]\mathbf{w}}{2R_L} \tag{2.38}$$

$$= \frac{\mathbf{w}^H \mathbf{R}_v \mathbf{w}}{2R_L}, \tag{2.39}$$

$$P_{v,av} = \alpha \frac{\mathbf{w}^H \mathbf{R}_v \mathbf{w}}{2R_L}. \tag{2.40}$$

In order to determine the proportionality constant α we set the available power due to a spatially isotropic noise environment with the antenna in equilibrium with its environment, $P_{te,av}$, equal to the available power from a single port antenna under the same conditions [23]

$$P_{te,av} = \alpha \frac{\mathbf{w}^H \mathbf{R}_{te} \mathbf{w}}{2R_L} = k_b T_{iso} B_n. \tag{2.41}$$

The proportionality constant can be found by rearranging Equation (2.41). Putting the constant into Equation (2.40), the available power at the antenna terminals is

$$P_{v,av} = k_b T_{iso} B_n \frac{\mathbf{w}^H \mathbf{R}_v \mathbf{w}}{\mathbf{w}^H \mathbf{R}_{te} \mathbf{w}}. \tag{2.42}$$

The equivalent temperature is calculated from the available power in the usual way,

$$P_{v,av} = k_b T_v B_n. \tag{2.43}$$

Using Equations (2.43) and (2.42) the equivalent temperature can be written as

$$T_v = T_{iso}\frac{\mathbf{w}^H\mathbf{R}_v\mathbf{w}}{\mathbf{w}^H\mathbf{R}_{te}\mathbf{w}}. \tag{2.44}$$

2.5 Efficiencies

In this section the array will be described in terms of efficiencies, which is a helpful tool in understanding array performance. Aperture efficiency describes the overall efficiency of an aperture type antenna using the available power at the antenna terminals. It can be separated into various other efficiencies such as radiation, spillover, illumination, blockage and diffraction, and surface accuracy efficiencies, etc. [23], [25], [14], [29]. There are also efficiencies that describe how well the antenna is matched to the receiver; for example, noise matching efficiency describes how much the LNA noise increases due to impedance mismatch [24]. In the following sections aperture, spillover, radiation, and noise matching efficiencies will be discussed.

2.5.1 Aperture Efficiency

Aperture efficiency, sometimes called antenna efficiency, will be defined as the ratio of effective area to the physical area of the aperture,

$$\eta_{ap} = \frac{A_e}{A_{phys}}, \tag{2.45}$$

where the effective area is the ratio of available output power from a signal of interest at the antenna terminals to incident power

$$A_e = \frac{P_{s,av}}{S^{sig,p}}, \tag{2.46}$$

$$\eta_{ap} = \frac{P_{s,av}}{S^{sig,p}A_{phys}}. \tag{2.47}$$

The available beamformer output power due to the signal of interest is

$$P_{s,av} = k_b T_{iso} B_n \frac{\mathbf{w}^H \mathbf{R}_s \mathbf{w}}{\mathbf{w}^H \mathbf{R}_{te} \mathbf{w}}. \tag{2.48}$$

Combining Equations (2.47) and (2.48) the aperture efficiency can be written as

$$\eta_{ap} = \frac{k_b T_{iso} B_n}{S^{sig,p} A_{phys}} \frac{\mathbf{w}^H \mathbf{R}_s \mathbf{w}}{\mathbf{w}^H \mathbf{R}_{te} \mathbf{w}}. \tag{2.49}$$

2.5.2 Spillover Efficiency

From the perspective of a transmitting antenna spillover efficiency is a measure of how much power from the feed of a reflector is actually incident on the reflector. From a receiving antenna perspective it describes how much thermal noise is received from the ground because the feed's receiving pattern spills over the edge of the reflector. From [22] it can be shown that the spillover efficiency is

$$\eta_{sp} = 1 - \frac{T_{iso}}{T_g} \frac{\mathbf{w}^H \mathbf{R}_{sp} \mathbf{w}}{\mathbf{w}^H \mathbf{R}_{iso} \mathbf{w}}. \tag{2.50}$$

2.5.3 Radiation Efficiency

For a receiving array the radiation efficiency is the ratio of power received from a spatially isotropic noise environment if $\mathbf{R}_{A,ohmic} = 0$ to power received from a spatially isotropic noise environment when the antenna is in thermal equilibrium with its environment. This can be expressed as

$$\eta_{rad} = \frac{\mathbf{w}^H \mathbf{R}_{iso} \mathbf{w}}{\mathbf{w}^H \mathbf{R}_{te} \mathbf{w}}. \tag{2.51}$$

The effect of the array not being in thermal equilibrium is taken into account when calculating the system noise temperature increase caused by the antenna losses, as in Equation (2.59)

2.5.4 Noise Matching Efficiency

From Equation (2.44) we can say that the beam equivalent temperature due to the noise introduced by the LNAs is

$$T_{lna} = T_{iso}\frac{\mathbf{w}^H\mathbf{R}_{lna}\mathbf{w}}{\mathbf{w}^H\mathbf{R}_{te}\mathbf{w}}. \tag{2.52}$$

The noise matching efficiency is the ratio of the minimum possible T_{lna} to the actual T_{lna},

$$\eta_n = \frac{T_{lna,min}}{T_{lna}}. \tag{2.53}$$

If $\mathbf{T}_{min}$ is a scaled identity matrix then $\mathbf{T}_{min} = \mathbf{I}T_{min}$ and $T_{lna,min} = T_{min}$.

2.6 Signal to Noise Ratio and Sensitivity

An important figure of merit for a phased array is the signal to noise ratio (SNR), which is a ratio of powers. In terms of the correlation matrices already defined the signal to noise ratio is

$$\begin{aligned}
\text{SNR} &= \frac{\mathbf{w}^H\mathbf{R}_s\mathbf{w}}{\mathbf{w}^H\mathbf{R}_n\mathbf{w}} && (2.54)\\
&= \frac{\mathbf{w}^H\mathbf{R}_s\mathbf{w}}{\mathbf{w}^H(\mathbf{R}_t + \mathbf{R}_{loss} + \mathbf{R}_{rec})\mathbf{w}}, && (2.55)\\
&= \frac{P_{s,av}}{P_{n,av}} && (2.56)\\
&= \frac{A_e S^{sig,p}}{k_b T_n B_n}, && (2.57)
\end{aligned}$$

where T_n, which is often called T_{sys}, is the beam equivalent noise temperature of the entire system. From Equation (2.57) it can be seen that another figure of merit can be A_e/T_{sys}, which is the SNR normalized by the signal amplitude. Rearranging

Equation (2.57) results in

$$S_{sys} \stackrel{\text{def}}{=} \frac{A_e}{T_{sys}} = \frac{k_b B_n}{S^{sig,p}} \text{SNR}, \tag{2.58}$$

where S_{sys} is the system sensitivity in units of m^2/K. Using the definitions of the correlation matrices and assuming that $\mathbf{R}_t = \mathbf{R}_{sp}$ it can be shown that A_e/T_{sys} can be written in terms of efficiencies

$$\frac{A_e}{T_{sys}} = \frac{\eta_{ap} A_{phys}}{\eta_{rad}(1-\eta_{sp})T_g + (1-\eta_{rad})T_a + T_{rec}}. \tag{2.59}$$

Another common figure of merit in radio astronomy, which is also often times called the sensitivity, is the smallest flux density that can be detected by the antenna, $\Delta F^{sig,p}$, which is

$$\Delta F^{sig,p} = \frac{k_b T_{sys}}{A_e 10^{-26}} \text{SNR} \frac{1}{\sqrt{B_n t}}, \tag{2.60}$$

where t is the integration time. A longer integration time corresponds to averaging the sampled correlation matrix in Equation (2.4) for more time samples. Variations in receiver gain provides a practical limit on the benefit of integration time [1].

It has been shown that the various contributions to the output of a PAF can be understood in terms of signal and noise correlation matrices, which provide a convenient way to define efficiencies and equivalent noise temperatures. The efficiencies and noise temperatures are used to understand system performance. Chapter 3 describes the two models used to simulate a 19 element hexagonal dipole PAF in software. Chapter 4 compares many of the parameters mentioned in the above sections, such as the array impedance, individual element receive patterns, efficiencies, and sensitivity, for the models and the prototype PAF.

Chapter 3

Phased Array Feed Model

This chapter describes the approach used to model the 19 hexagonal array of dipoles that was recently built and tested as a prototype phased array feed for radio astronomy. This chapter will focus mainly on the finite element method (FEM) numerical model of the array that was created using HFSS (Ansoft Corp.). An analytical, sinusoidal current model will also be described.

3.1 HFSS Array Model

3.1.1 Dimensions and Materials

Figures 3.1 and 3.2 show the PAF model in HFSS. The ground plane and the dipoles are modeled as perfect electric conductors, which leads to a radiation efficiency of 100%. The radiation box that surrounds the array is filled with free space, and the structure surrounding the radiation box is a perfectly matched layer (PML). The PML enable the fields produced by the array to radiate outward with very little reflection, which results in valid radiated fields.

The dimensions of the 19 element PAF are similar to the dimensions of the prototype PAF: the element spacing is $0.6\lambda_0$, where λ_0 is the wavelength corresponding to a design frequency of 1.6 GHz and is approximately 18.7 cm.

Figure 3.3 shows the HFSS model of an individual element in the array. The dimensions of the individual elements are also similar to the dimensions of the prototype elements.

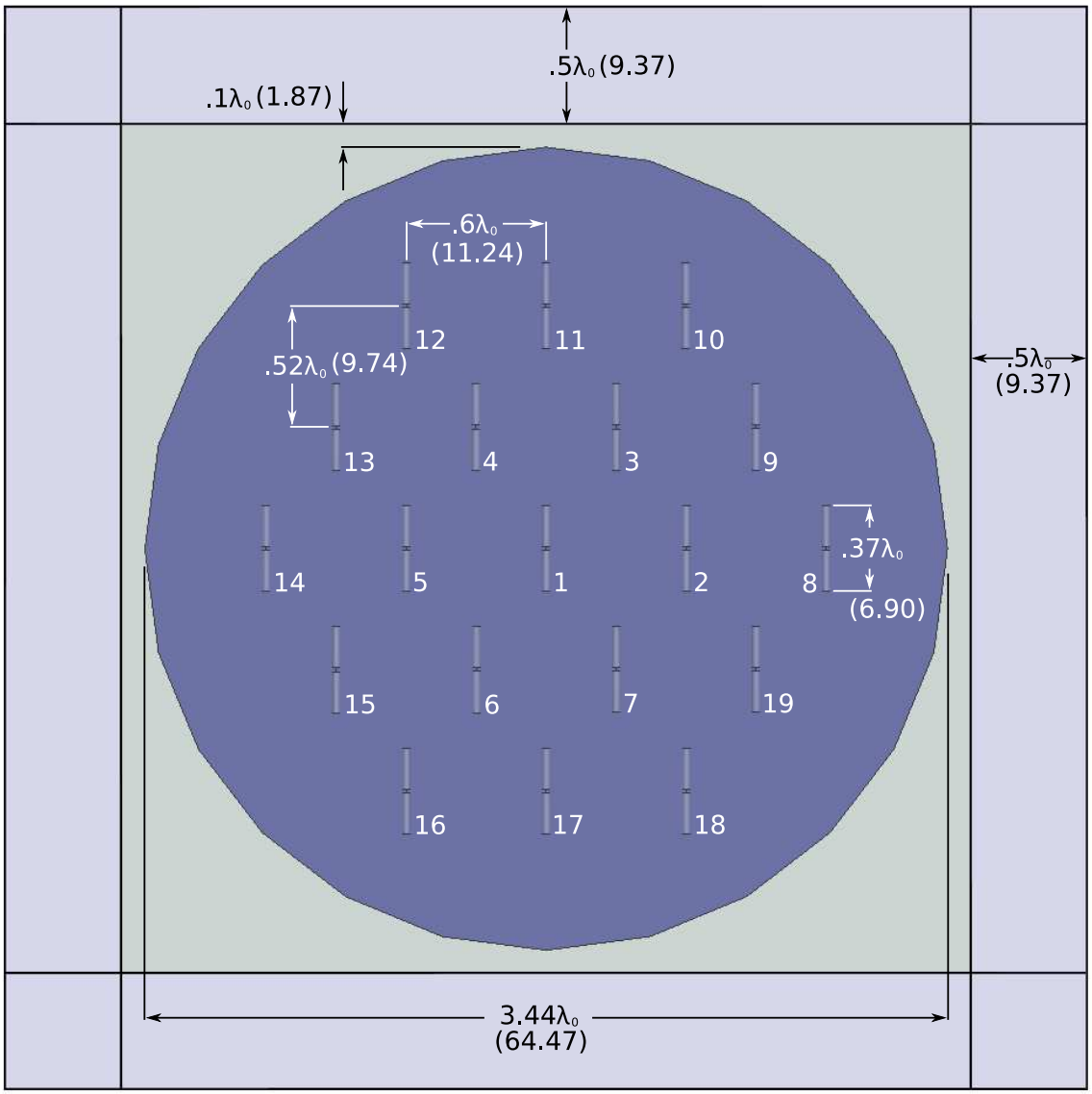

Figure 3.1: Front view of the FEM model of the 19 element thickened dipole PAF. $\lambda_0 = 18.74$cm is the free space wavelength corresponding to a frequency of 1.6 GHz, dimensions in $(\cdot)$ have units of cm. The numbers next to each element indicate the element numbering used in the HFSS model.

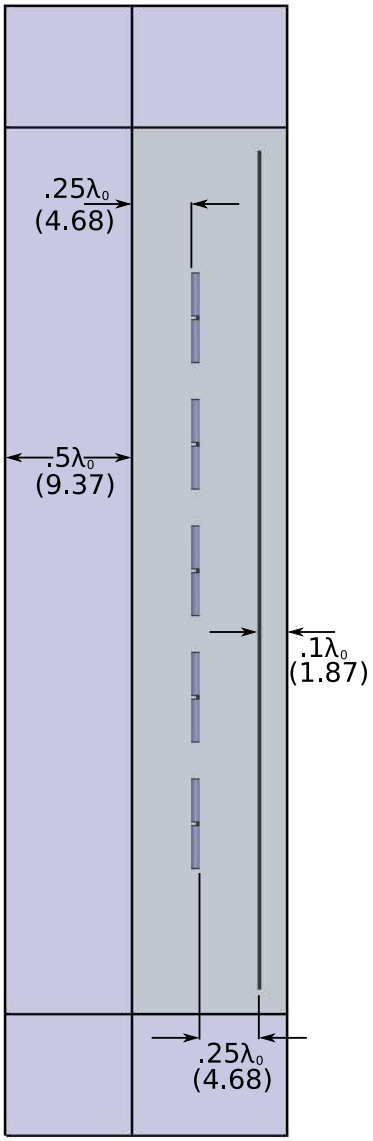

Figure 3.2: Side view of the FEM model of the 19 element thickened dipole PAF. The PML surrounds the array on all sides except directly behind the ground plane. $\lambda_0 = 18.74$cm is the free space wavelength corresponding to a frequency of 1.6 GHz, dimensions in $(\cdot)$ have units of cm.

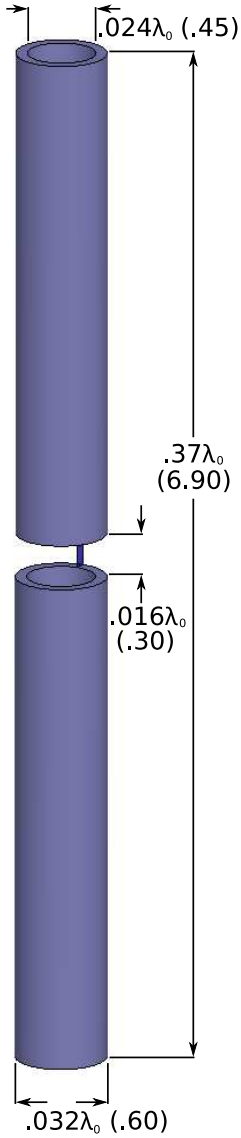

Figure 3.3: FEM model of an element in the 19 element thickened dipole PAF. $\lambda_0 = 18.74$cm is the free space wavelength corresponding to a frequency of 1.6 GHz, dimensions in $(\cdot)$ have units of cm.

3.1.2 Accuracy

An important consideration when using a numerical method such as the finite element method that HFSS uses is the accuracy of the results. The most definitive comparisons for accuracy are usually comparisons with measured results, however, there are some simple checks on the results that are necessary for accuracy but are insufficient to know exactly how accurate the results are.

One necessary condition for accuracy is conservation of energy, which can easily be checked in the case of lossless antennas. Since energy must be conserved and there is no loss in the system, the power radiated by the antenna array, P_{rad}, should equal the power incident on its feed ports, P_{in}. From Equations (2.17) and (2.18) the following relation should hold for conservation of energy.

$$\mathbf{R}_A = \frac{2}{|I_0|^2}\mathbf{A}. \tag{3.1}$$

Figure 3.4 shows the difference between the overlap matrix and the real part of the impedance matrix for the 19 element array simulated in HFSS.

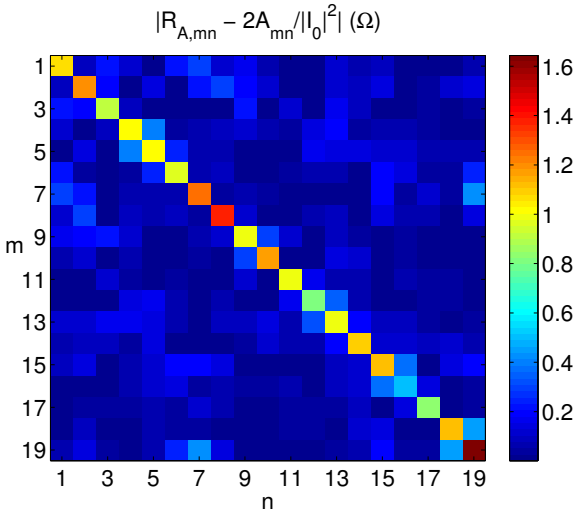

Figure 3.4: Difference between the real part of the array impedance matrix and the overlap matrix, both obtained with the HFSS model. For a lossless array this difference should be zero.

Another check for accuracy is the solution convergence. HFSS adaptively solves for the fields in the region by iteratively increasing the number of mesh elements and solving for the fields until the change in energy from one solution to the next is less than a parameter specified by the user. A more convergent solution would, in general, be more accurate than a less convergent solution. For the array model using the current source feed type the maximum change in energy was set to 0.02.

3.1.3 Feed Structure

As can be seen in Figure 3.3 a feed gap source was used to model the feed structure. The feed gap source is much simpler than modeling the coaxial feed and quarter wave balun and requires much fewer tetrahedra for the FEM mesh. However, the feed gap source does not incorporate the effect of the balun as the frequency of operation moves away from the center design frequency of 1.6 GHz. The additional accuracy that could be obtained compared to the additional number of tetrahedra which would be required to model the balun was not examined.

3.1.4 Radiation Boundary

A radiation boundary is defined on the faces of the radiation box. These faces are also touching the PML, with the exception of the face that lies behind the ground plane. A simpler radiation boundary condition, the absorbing boundary condition (ABC), is used behind the ground plane to save computation time because very little energy is radiated in that direction.

3.1.5 Ground Plane

The ground plane in the HFSS model is modeled as a perfect electric conductor (PEC) with no thickness. The ground plane is not modeled as an infinite ground plane, therefore edge diffraction is taken into account and the electric fields are non-zero behind the ground plane.

3.1.6 Source Type

One source type that is used in modeling the feed gap source is a constant current source. The magnitude and phase of the current can be changed in post-processing which allows for the transmit fields to be found for individual elements by scaling the magnitude of one current source to unity while scaling the others to zero. The self and mutual impedances of the ports are obtained by creating a line on each source before simulation and by integrating the tangential component of the electric field along that line to get the voltage in post-processing in HFSS. The mutual

impedance $Z_{A,mn}$ is found by dividing the voltage at port m by the current at port n when the current at all the other ports is zero. The impedance $Z_{A,mm}$ is similarly found by dividing the voltage at port m by the current at port m when all the other currents are zero. This type of port was used to generate the radiation patterns of the individual elements, see Section 4.2 and to generate the array impedance matrix at 1600 MHz, see Section 4.1.6.

The lumped port is another type of source that is useful in modeling the feed gap source. With the lumped port the voltage integration line is defined at the time the source is created and the self and mutual impedances are calculated by HFSS, and the user specifies simulation convergence by setting a maximum change in the S-parameters between successive adaptive passes. The lumped port was used to determine the impedance matrix of the array as function of frequency, see Sections 4.1.2–4.1.5.

It should be noted that when using lumped port sources to obtain radiation patterns, when one port is active the other ports are loaded. This would need to be taken into account in determining the array receive pattern in Equation (2.6) because Equation (2.5) assumes that the radiation pattern of one element in the array is obtained when the other elements are open circuited. Using a lumped port source to obtain radiation patterns was not done for the results presented in Chapter 4, but it is an option for future PAF models.

3.2 Analytical Array Model

An analytical model is used for comparisons with the HFSS model to quantify the benefit of using the more complicated numerical modeling software. The analytical model used is well known in the literature [25]. The model assumes a sinusoidal current distribution along the length of the dipole and a very thin dipole. The ground plane is assumed to be infinite. The analytical model also assumes that the individual element patterns are not affected by the other elements in the array when calculating the open circuit voltages, $\check{\mathbf{v}}$, however, the mutual coupling is still taken into account when converting to voltages across a load, see Equations (2.6) and (2.7). As with the

HFSS model the elements are assumed to be lossless. The array impedance matrix is assumed to be purely real and it is obtained by calculating the overlap matrix.

Chapter 4

Comparing PAF Models with Measured Results

This chapter compares several antenna parameters of the two PAF models described in the previous chapter (the HFSS and analytical array models) with measured results. The parameters compared in this chapter include those related to the array impedance matrix, $\mathbf{Z}_A$ and the scattering matrix, $\mathbf{S}_A$; the bare array receive patterns of the individual array elements and of a simple beamformer; the sensitivity, efficiency, and system temperatures of the PAF mounted on the Green Bank, WV 20 meter telescope; and the signal and noise correlation matrices of the PAF mounted on the same telescope.

4.1 Impedance and Scattering Matrix

This section compares several parameters related to the array impedance matrix, $\mathbf{Z}_A$ and the scattering matrix, $\mathbf{S}_A$ over a range of frequencies and at 1600 MHz.

4.1.1 A Note About the Measured Results

The measured results presented in Sections 4.1.2–4.1.5 are from a seven element array of similar construction to the nineteen element array. This array is described by James Nagel in [30] and some of the measured results shown here are also shown his work in a different form and they are repeated here for comparison to the models. Reflection and transmission coefficient measurements were taken using a two port network analyzer. The reflection coefficients of the antennas were measured one at a time using only one port of the network analyzer, and the other antennas were terminated in open circuits. The transmission coefficients of each antenna pair were measured with the other five antennas terminated in open circuits.

All of the measured results are combined into a matrix $\mathbf{S}_A^{oc}$, where the $(\cdot)^{oc}$ represents the fact that the measurements were taken with open circuit terminations on the antennas not being tested with the two port network analyzer. It should be noted that $\mathbf{S}_A^{oc}$ is not the multiport scattering matrix of the array because of the open circuit terminations. The multiport scattering matrix is defined as

$$\mathbf{S}_A = (\mathbf{Z}_A + \mathbf{I}Z_0)^{-1}(\mathbf{Z}_A - \mathbf{I}Z_0), \tag{4.1}$$

where $Z_0 = 50\Omega$ is the characteristic impedance of each port and $\mathbf{I}$ is the identity matrix.

It can be shown that the elements of $\mathbf{S}_A^{oc}$ can be defined in terms of $\mathbf{S}_A$ by [31]

$$\begin{aligned} \mathbf{S}'_A(m,n) &= (\mathbf{I} - \mathbf{S}_A)^{-1}(\mathbf{S}_A - \mathbf{\Gamma}(m,n))(\mathbf{I} - \mathbf{S}_A\mathbf{\Gamma}(m,n))^{-1}(\mathbf{I} - \mathbf{S}_A), \\ S^{oc}_{A,mn} &= S'_{A,mn}(m,n), \end{aligned} \tag{4.2}$$

where $\mathbf{\Gamma}(m,n)$ is a diagonal matrix of reflection coefficients for the array when elements m and n are being tested and the other elements are open circuited,

$$\Gamma_{aa}(m,n) = \begin{cases} 0 & \text{if } a = \{m,n\}, \\ 1 & \text{otherwise.} \end{cases} \tag{4.3}$$

It should also be noted that the measurements were not taken in an anechoic chamber.

A separate HFSS model was created with seven elements and a smaller ground plane to match the actual seven element array. Also, the seven element HFSS model used lumped port sources as opposed to current sources. The difference between these two types of sources is described in Section 3.1.6.

4.1.2 Voltage Standing Wave Ratio

The voltage standing wave ratio (VSWR) is a well known parameter that describes the amount of reflection from a port. For our purposes we will define the

VSWR of the mth element, when all other elements are terminated in open circuits to be

$$\text{VSWR}_m = \frac{1 + |S^{oc}_{A,mm}|}{1 - |S^{oc}_{A,mm}|}. \tag{4.4}$$

The measured and modeled VSWR is shown in Figure 4.1. The bandwidth of an antenna is usually considered to be the frequencies over which the VSWR is less than 2. The range of frequencies shown in Figure 4.1 was chosen to match the bandwidth of the receiver system [30].

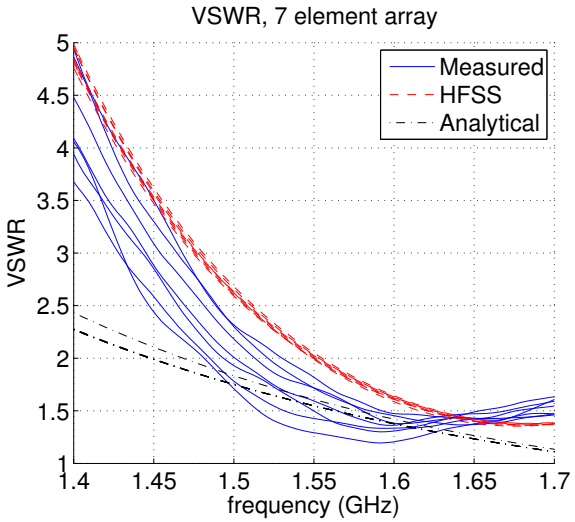

Figure 4.1: Modeled and measured VSWR for each element in the seven element array.

4.1.3 Self Impedances vs. Frequency

Using the same seven element array measured results and models mentioned in Section 4.1.1, the self impedance of the mth element when all other elements are terminated in open circuits is

$$Z^{oc}_{Amm} = Z_0 \frac{1 + S^{oc}_{Amm}}{1 - S^{oc}_{Amm}}. \tag{4.5}$$

The self impedances are shown in Figure 4.2, both the model and the measurements show that the resistive part is near 50 Ω, and that there is a significant reactive part.

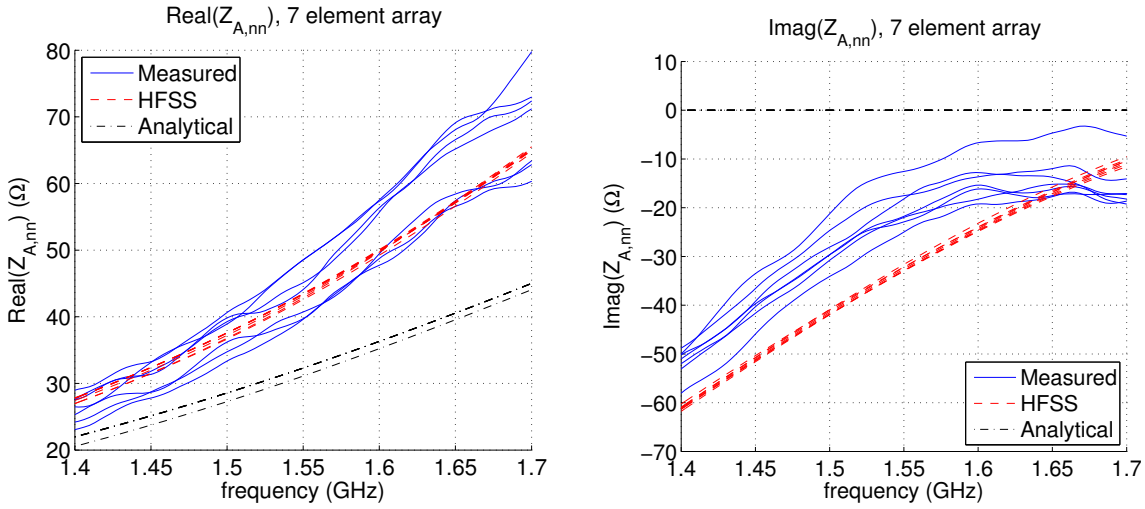

(a) Real

(b) Imaginary

Figure 4.2: Measured and modeled self impedances for each element in the seven element array. (a): Re $\left(\mathbf{Z}^{\text{oc}}_{\text{A,nn}}\right)$. (b): Im $\left(\mathbf{Z}^{\text{oc}}_{\text{A,nn}}\right)$.

4.1.4 Coupling (Transmission Coefficients) vs. Frequency

One gauge of the amount of coupling between two antennas is the transmission coefficient, which is a measure of how much an incident voltage wave on one antenna's terminals is transmitted to the other antenna's terminals.

The coupling between two antennas is strongly dependent on their arrangement relative to each other. Therefore, all the pairs of dipoles in an array that have similar arrangements tend to have similar coupling. For the seven element array mentioned in Section 4.1.1 there are six unique dipole pair arrangements. The magnitudes and phases of the transmission coefficients are shown in Figures 4.3–4.4, with each plot corresponding to a different arrangement of dipoles. In addition to the relative positions of the two dipoles, the presence and locations of the other dipoles in the

array also affect the coupling between the two dipoles, however, this is a second order effect.

The differences may be caused by approximations in the HFSS model such as the absence of the feed structure, and the fact that the measurements were not taken in an anechoic chamber.

4.1.5 Reflection Coefficients vs. Frequency

Figure 4.5 shows the reflection coefficient, $S^{oc}_{A,mm}$ of the individual elements for the HFSS model and the measured results for the seven element array.

4.1.6 Transmission and Reflection Coefficient Matrix at 1600 MHz

Figure 4.6 compares the structure $\mathbf{S}^{oc}_{A}$ for the seven element HFSS model and the measurements at the center frequency (1600 MHz) by showing the magnitudes of the elements in the matrix. There are similarities in the overall pattern and in the values of several elements in the matrix, however, the values of several elements in the array are significantly different. The similarities and differences are expected based on the similarities and differences seen in Figures 4.3 and 4.5.

Figure 4.7 shows the structure of $\mathbf{Z}_A$ for the 19 element HFSS model and analytical model. The agreement in overall structure of $\mathrm{Re}\,(\mathbf{Z}_\mathrm{A})$ between the two models is very good, however, the values appear to be different by a scale factor. The analytical model assumes that $\mathbf{Z}_A$ is purely real.

4.2 Bare Array Receive Patterns

The bare array receive patterns for the 19 element array were measured by Jonathan Landon at the NRAO site at Green Bank, WV. Similar measurements were taken for the seven element array by James Nagel and are described in [30]. For the 19 element array measurements, the vector $\mathbf{v}$ of received voltages was measured and the correlation matrix was computed as a function of angle. E-plane and H-plane cuts were measured.

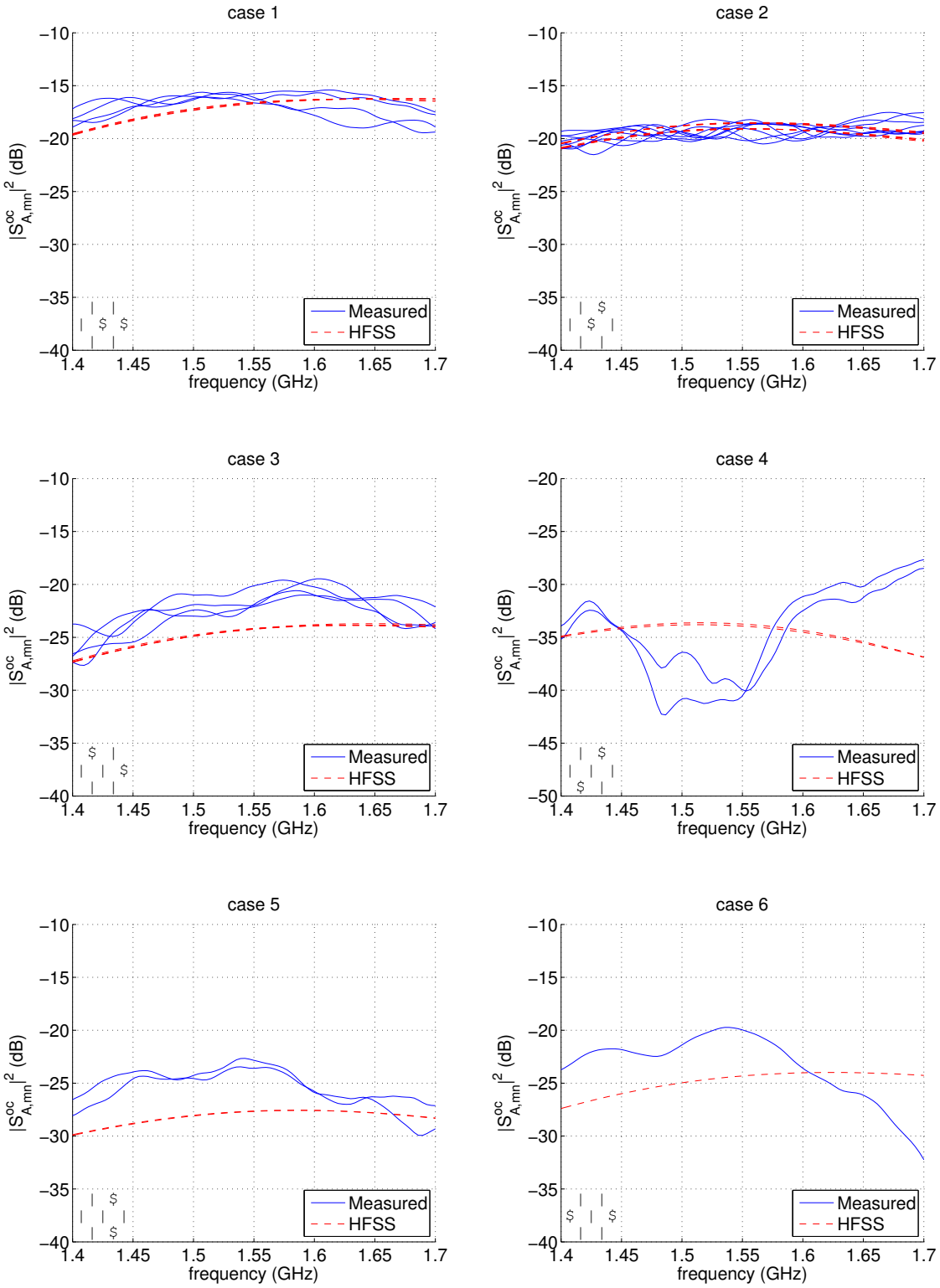

Figure 4.3: Magnitude of transmission coefficients versus frequency. All the dipole pairs that have similar arrangements share the same plot, an example of the arrangement is shown in the lower left hand corner of each plot.

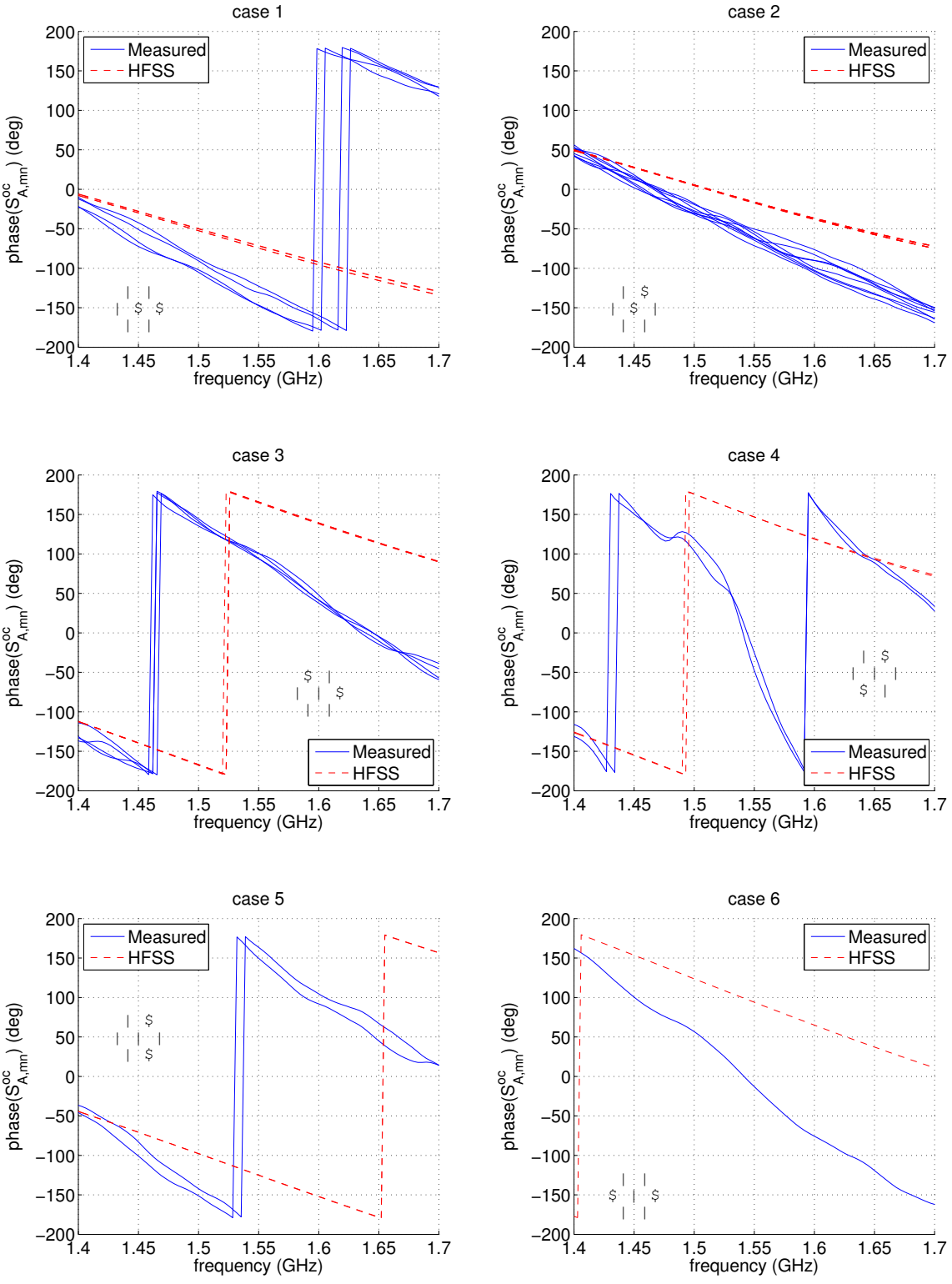

Figure 4.4: Phase of transmission coefficients versus frequency. All the dipole pairs that have similar arrangements share the same plot, an example of the arrangement is shown in the lower left hand corner of each plot.

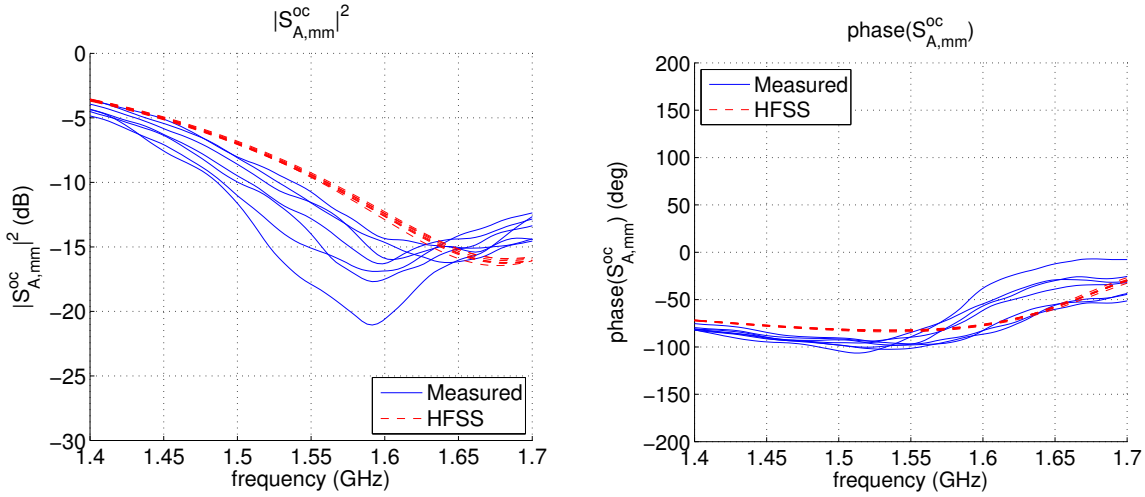

Figure 4.5: Magnitude and phase of the diagonal elements of $\mathbf{S}_A^{oc}$ versus frequency.

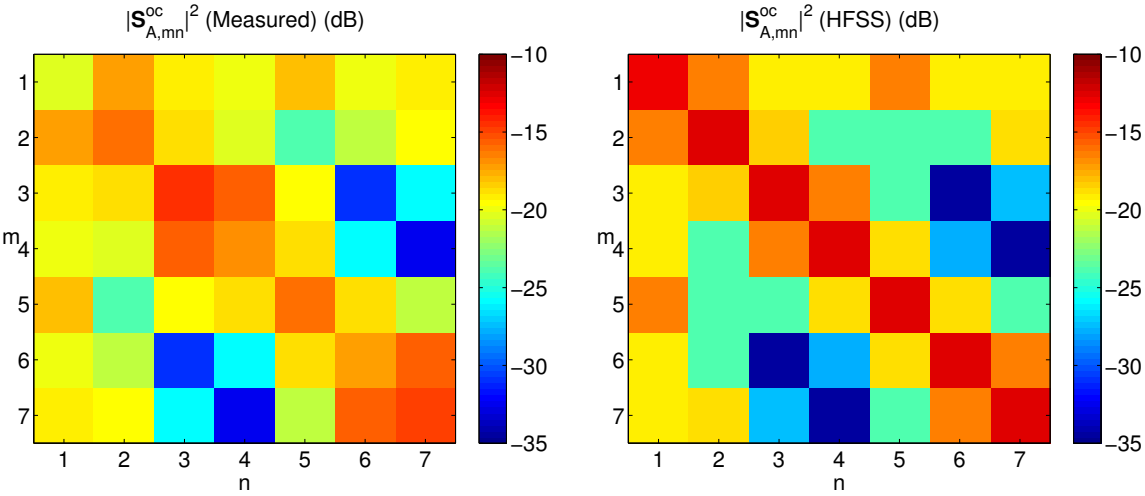

Figure 4.6: Matrix view of the magnitude of the elements of $\mathbf{S}_A^{oc}$ at 1600 MHz.

The E and H-plane receive patterns were also modeled using the HFSS and analytical models. The models assume that the received signal strength is large enough that the noise correlation matrices can be ignored. This may not be a good approximation as the angle away from boresight becomes large in the E-plane cut.

Figures 4.8–4.11 show the magnitudes of the diagonal elements of $\mathbf{R}_v$. The values in each pattern were scaled so that the maximum value was unity. The coordinate system is described in Appendix A. Several of the plots in the figures have

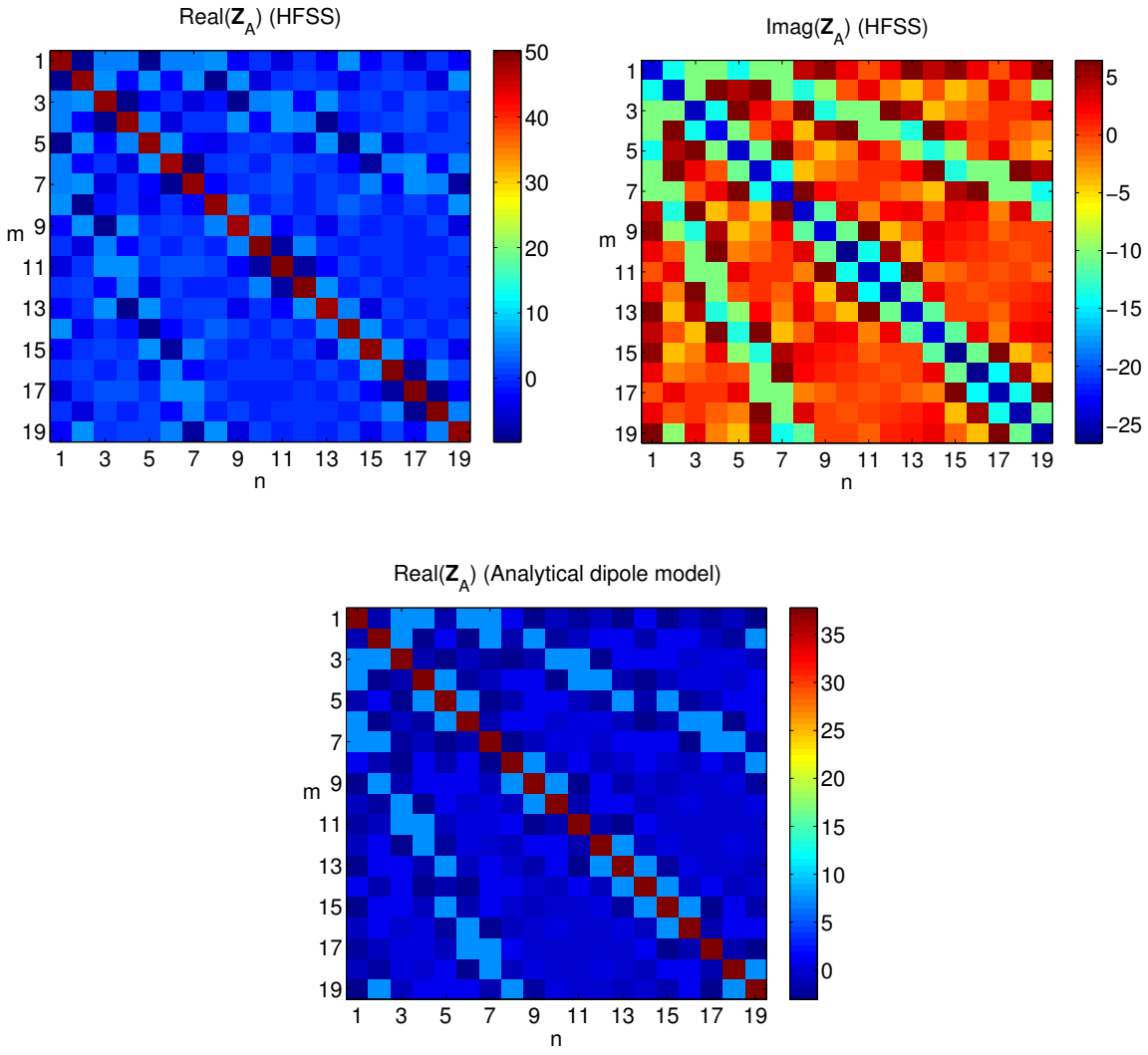

Figure 4.7: Matrix view of the array impedance matrix for the HFSS and analytical models at 1600 MHz.

two element patterns, this is because their locations on the array are symmetric with respect to the particular cut (E or H-plane).

There are many similarities between the models and the measured patterns, the HFSS model seems to capture much of the overall shape of the measured patterns especially with the E-plane cuts between $\pm 60°$ and the H-plane between $\pm 80°$.

A significant difference between the analytical model and the other two plots in Figures 4.8–4.11, is that the analytical receive pattern for each element is symmetric.

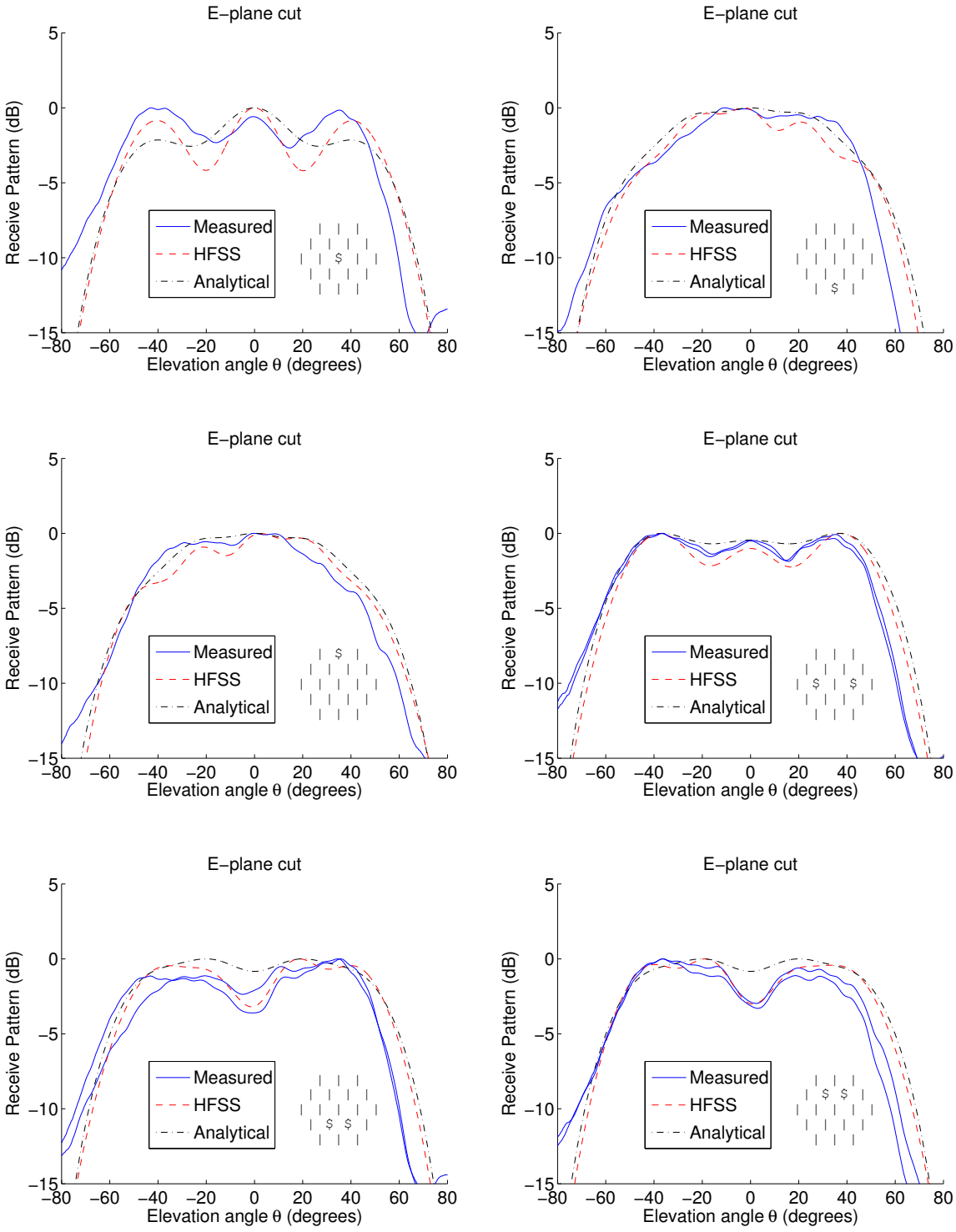

Figure 4.8: Receive patterns of individual elements, E plane cut. All plots are normalized to have an equal peak value. The element(s) is depicted by the $ in the right hand corner of each plot.

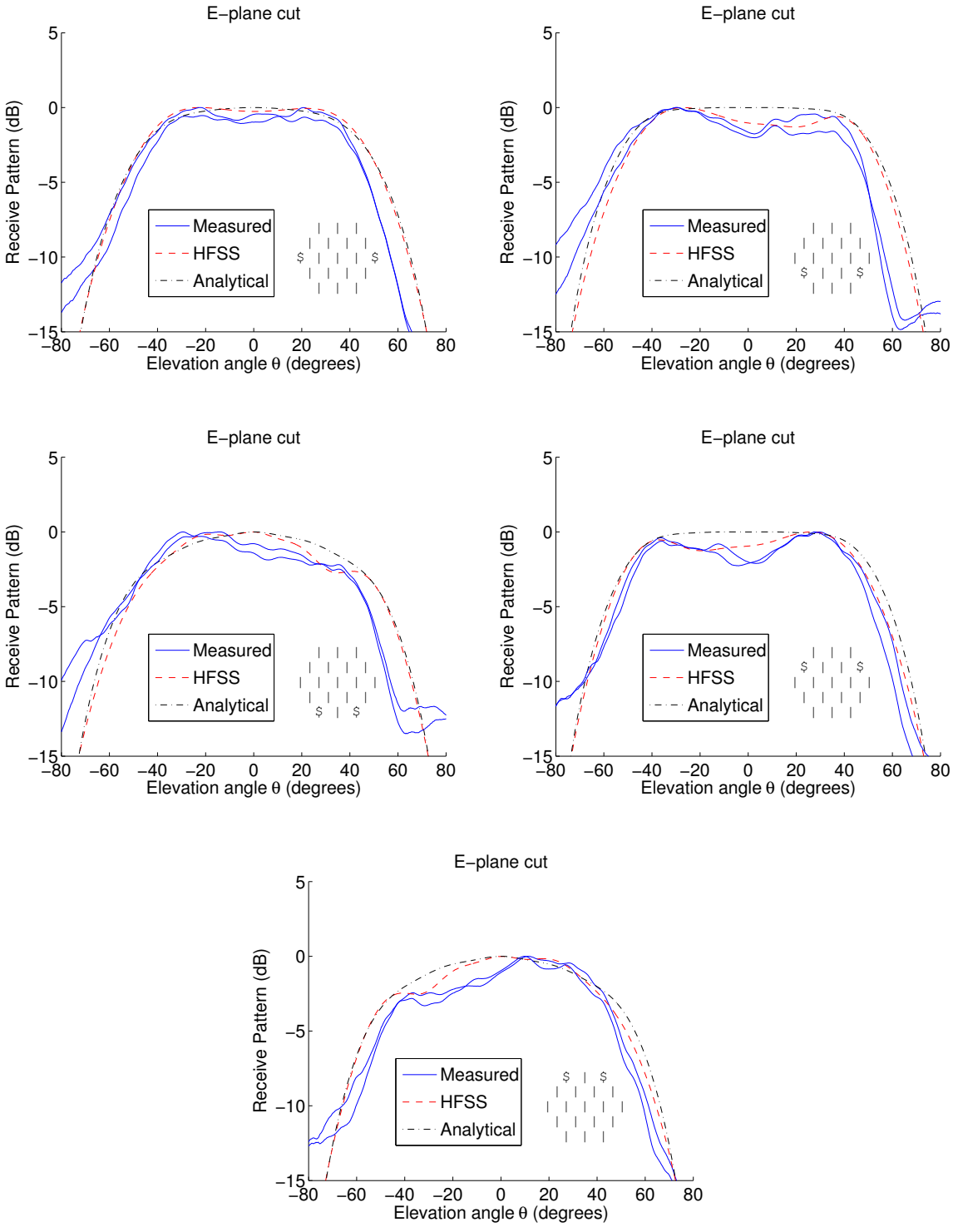

Figure 4.9: Receive patterns of individual elements, E plane cut. All plots are normalized to have an equal peak value. The element(s) is depicted by the $ in the right hand corner of each plot.

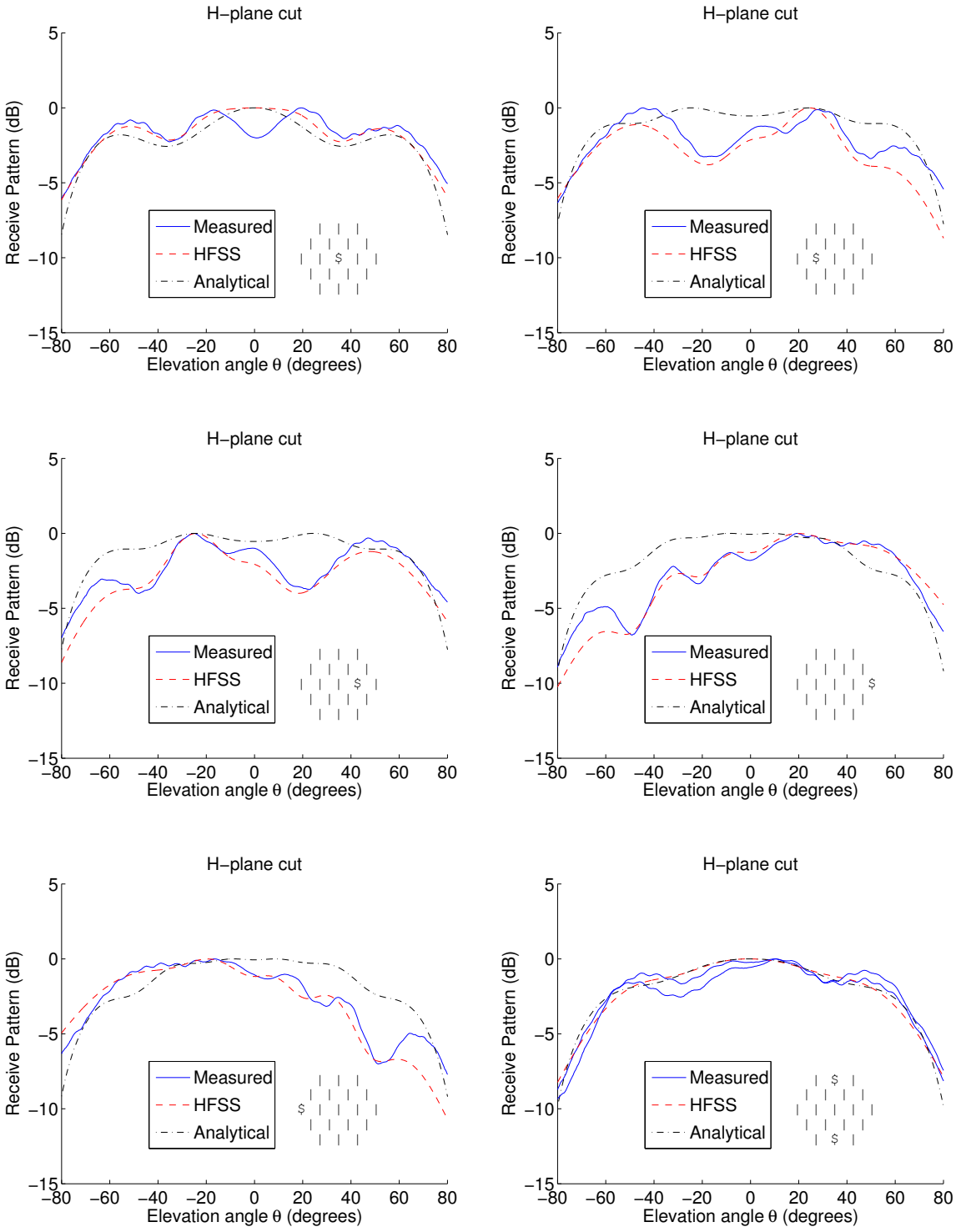

Figure 4.10: Receive patterns of individual elements, H plane cut. All plots are normalized to have an equal peak value. The element(s) is depicted by the $ in the right hand corner of each plot.

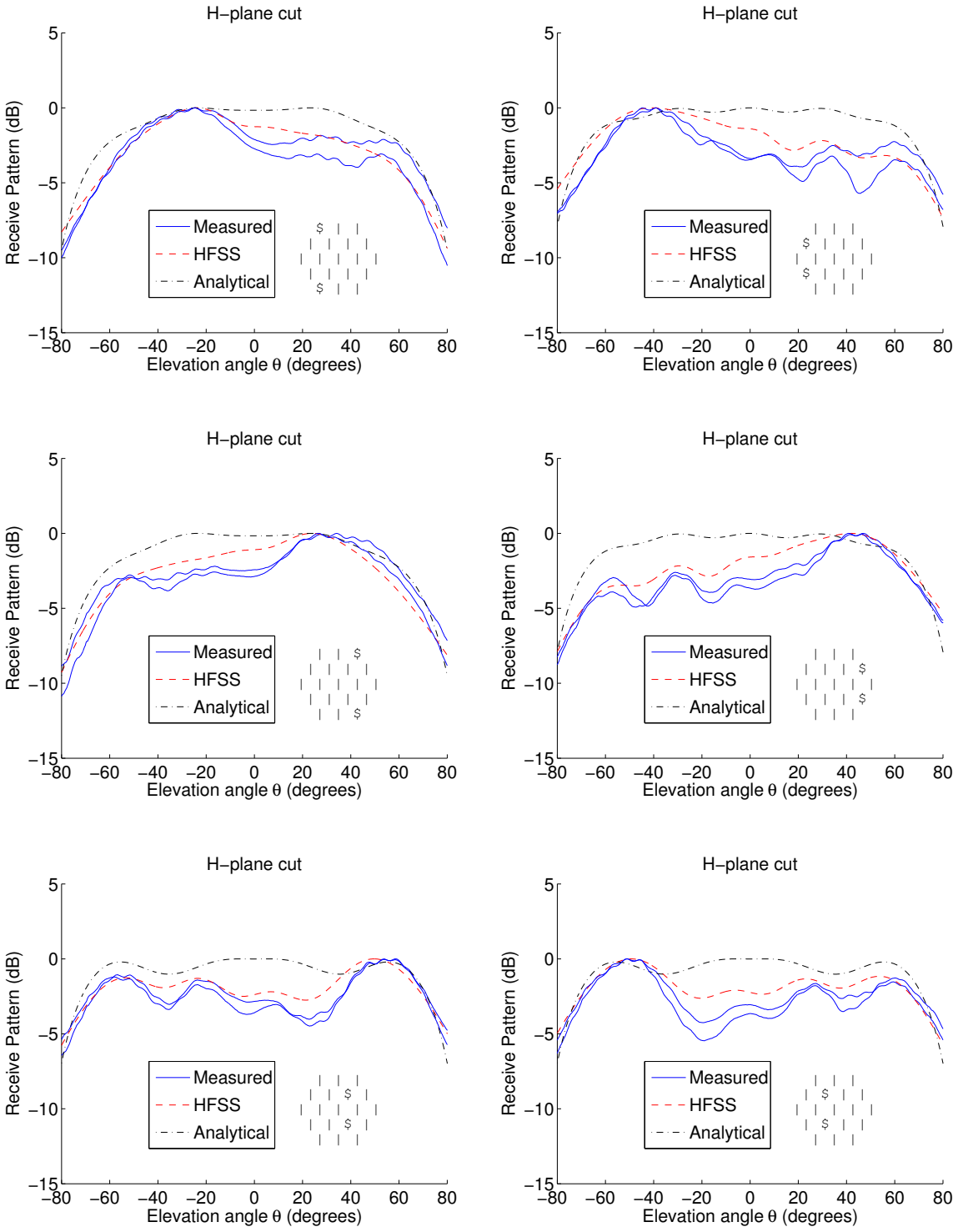

Figure 4.11: Receive patterns of individual elements, H plane cut. All plots are normalized to have an equal peak value. The element(s) is depicted by the $ in the right hand corner of each plot.

This is to be expected because the analytical radiation patterns assume that the individual elements are isolated. The analytical model does not completely ignore the presence of all the elements in array because mutual coupling is still taken into account in the transformation of open circuit voltages to loaded voltages by the matrix $\mathbf{Q}$ as in Equation (2.6). If mutual coupling were completely ignored the received voltages would be the radiation pattern of a single dipole above a ground plane.

There are also significant differences between the HFSS model and the measured results, especially in the E-plane cut when the angle off from boresight is greater than 60°. This may be due to the assumption that the signal strength is large enough that the noise correlation matrices can be ignored, which would be less likely to be accurate as the angle increases. This affect would also be stronger in the E-plane cut than in the H-plane cut since for an isolated dipole there are nulls in the receive pattern at $\theta = \pm 90°$ in the E-plane, but the pattern is more constant in the H-plane.

A conjugate field match beamformed pattern was created in post processing. The weights, $\mathbf{w}$, are set equal to the eigenvector corresponding to the maximum eigenvalue of $\mathbf{R}_v$ when $\theta = 0$. The beamformed patterns in the E and H planes are shown in Figure 4.12. The values in each pattern were scaled so that the maximum value was unity. Also, the gains of the individual channels are normalized to unity in the case of the measured results.

The beamformed patterns in the H-plane match well to the first sidelobes and the beamformed patterns in the E-plane match well in the main beam.

4.3 Figures of Merit

As mentioned in Sections 2.5–2.6 common figures of merit for a reflector antenna are the system temperature, T_{sys}, spillover efficiency, η_{sp}, aperture efficiency, η_{ap}, the system sensitivity, A_e/T_{sys}, and the receiver temperature, T_{rec}. These parameters will be compared for the experimental data and models. Equations for these parameters, which are easily obtained from equations in developed in Sections 2.4–2.6,

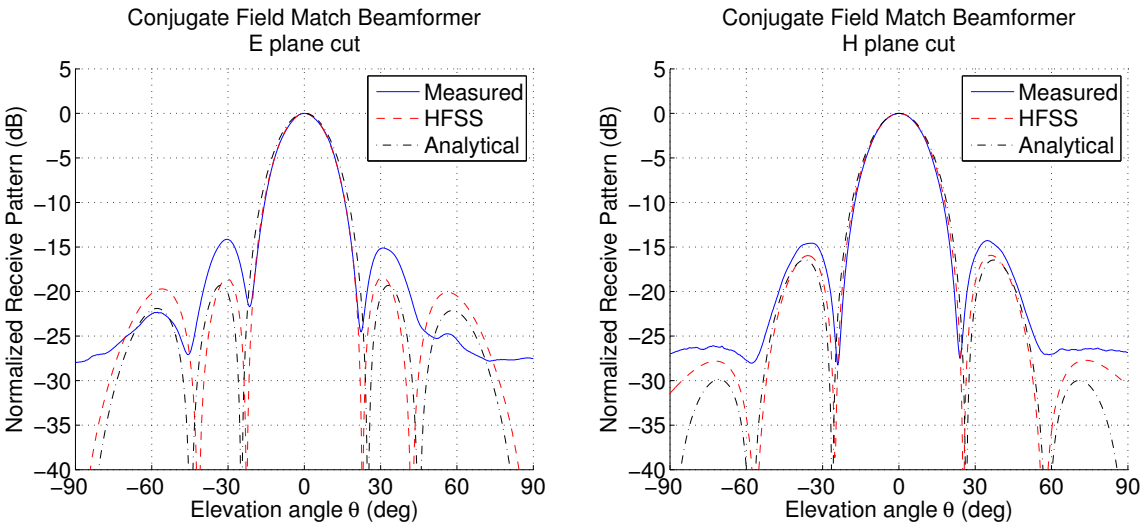

Figure 4.12: E and H-plane cuts of the receive pattern of the array using a conjugate field match beamformer at boresight. The plots are normalized to have an equal peak value.

are given below for convenience.

$$\begin{aligned}
\frac{A_e}{T_{sys}} &= \frac{k_b B_n}{S^{sig,p}} \frac{\mathbf{w}^H \mathbf{R}_s \mathbf{w}}{\mathbf{w}^H \mathbf{R}_n \mathbf{w}}, \\
A_e &= \frac{k_b T_{iso} B_n}{S^{sig,p}} \frac{\mathbf{w}^H \mathbf{R}_s \mathbf{w}}{\mathbf{w}^H \mathbf{R}_{te} \mathbf{w}}, \\
T_{sys} &= T_{iso} \frac{\mathbf{w}^H \mathbf{R}_n \mathbf{w}}{\mathbf{w}^H \mathbf{R}_{te} \mathbf{w}}, \\
\eta_{sp} &= 1 - \frac{T_{iso}}{T_g} \frac{\mathbf{w}^H \mathbf{R}_{sp} \mathbf{w}}{\mathbf{w}^H \mathbf{R}_{iso} \mathbf{w}}, \\
T_{rec} = T_{lna} &= T_{iso} \frac{\mathbf{w}^H \mathbf{R}_{lna} \mathbf{w}}{\mathbf{w}^H \mathbf{R}_{te} \mathbf{w}}.
\end{aligned} \tag{4.6}$$

Of the figures of merit mentioned only A_e/T_{sys} was obtained directly using the experimental data. A_e and T_{sys} are estimated using the HFSS model and the experimental data to make assumptions about $\mathbf{R}_{te}$, A_e, or T_{sys}. The spillover efficiency and the receiver temperature are not estimated, but values are given for the HFSS and analytical models.

The experimental data was taken using the NRAO 20 meter dish in Green Bank, WV. Several people from BYU and the NRAO were involved in obtaining the

experimental results and the author would like to acknowledge their contributions. The project was under the direction of professors Karl Warnick and Brian Jeffs from BYU and Roger Norrod and Rick Fisher from the NRAO. Jonathan Landon from BYU supervised much of the hardware construction and installation and was involved in much of the data collection. Assistance was also provided by Jacob Waldron, Mike Elmer and Alan Stemmons from BYU, along with myself.

Table 4.1 describes the parameters of the experiment used to compare the figures of merit mentioned above. An on-off steering calibration was used to obtain the weight vector, $\mathbf{w}$.

Table 4.1: Parameters of the experiment related to Table 4.4.

Signal of interest	CygnusA (CygA)
Frequency	1600 MHz
F^{sig}	1380 Janskys
$F^{sig,p}$	690 Janskys
calibrator filename	/Nov02_2007/PassiveTests_2Nov07/corrBin/... CygA_10secOn_10secOff_corr.bin
filename	/Nov01_2007/PassiveTests_1Nov07/corrBin/... CygA_13offsets_20secDwells_halfbeamwidths... _110sec_new_corr.bin
Reflector diameter	20 meters
f/D	0.43
B_n	387.53 kHz

Table 4.2 describes the model parameters used to compare with the experiment. The results that use these parameters are shown in Table 4.4 and Figures 4.13–4.15. The LNA parameters were assumed to be identical for each LNA, the input impedance Z_L was assumed and the remaining three, T_{min}, Z_{opt}, and R_N were based on measurements of two LNAs with identical model numbers to those used in the experiment (Mini-Circuits ZEL-1217LN), see Table 4.3.

Table 4.4 describes the results of the comparison between the models and experiment data. Three columns are shown for the experimental results because three

Table 4.2: Parameters of the models used to simulate the experiment data.

Frequency	1600 MHz
F^{sig}	1380 Janskys
$F^{sig,p}$	690 Janskys
LNA T_{min}	85 K
LNA Z_{opt}	$41 + j5\Omega$
LNA R_N	5 Ω
LNA Z_L	50 Ω
Reflector diameter	20 meters
f/D	0.43
B_n	387.53 kHz
T_g	280 K (44° F)

Table 4.3: Measured noise parameters of two Mini-Circuits ZEL-1217LN LNAs [1].

	LNA #20	LNA #21
$Z_{opt}(\Omega)$	$41.40 + j5.05$	$40.96 + j4.72$
$R_N(\Omega)$	4.94	4.81
$T_{min}(K)$	85.3 $\pm$ 17.7	83.6 $\pm$ 17.6

different assumptions were made to determine A_e and T_{sys}. One assumption used $\mathbf{R}_{te} = \mathbf{R}_{te,HFSS}$ to compute A_e and T_{sys}, another assumption used $T_{sys} = T_{sys,HFSS}$ to compute A_e, and the third assumption used $A_e = .95A_{e,HFSS}$ to compute T_{sys}. The factor of .95 is used because the modeled aperture efficiency is larger than is usually realistic for a parabolic reflector. Three beamformers: maximum SNR, conjugate field match, and center element only, are used in the comparison because each of the figures of merit are beamformer dependent. The maximum SNR and conjugate field match beamformers are discussed in [19]. The center element beamformer is $w_n = 0$ for all $n \neq 1$.

The sensitivities obtained using the HFSS models are 30 to 46% larger than experimental results and those obtained using the analytical models are 79 to 103% larger. The estimates of A_e and T_{sys} match well in the two cases where $\mathbf{R}_{te} = \mathbf{R}_{te,HFSS}$ and $T_{sys} = T_{sys,HFSS}$.

[1] Measured under the direction of Dr. Leonid Belostotski at the University of Calgary.

Table 4.4: PAF figures of merit using experimental data and models [2].

	Measured Assume $\mathbf{R}_{te}$	Measured Assume T_{sys}	Measured Assume η_{ap}	HFSS	Analytical
Maximum SNR beamformer					
A_e/T_{sys} (m^2/K)	**1.29**	1.29	1.29	**1.80**	**2.58**
T_{sys} (K)	133	(143)	189	143	92.9
η_{ap} (%)	54.5	58.7	(77.7)	81.8	76.4
η_{sp} (%)	–	–	–	96.5	98.4
T_{rec} (K)	–	–	–	133	88
Conjugate field match beamformer					
A_e/T_{sys} (m^2/K)	**1.16**	1.16	1.16	**1.69**	**2.35**
T_{sys} (K)	155	(156)	215	156	110
η_{ap} (%)	57.2	57.8	(79.8)	84.0	81.8
η_{sp} (%)	–	–	–	90.5	93.1
T_{rec} (K)	–	–	–	129	90
Center element only beamformer					
A_e/T_{sys} (m^2/K)	**0.94**	0.94	0.94	**1.22**	**1.68**
T_{sys} (K)	176	(186)	231	186	147
η_{ap} (%)	52.5	55.5	(68.9)	72.5	78.3
η_{sp} (%)	–	–	–	78.8	82.3
T_{rec} (K)	–	–	–	126	97

4.4 Signal and Noise Correlation Matrices of PAF on Reflector

An additional comparison of the models and the measured results using the experimental data taken with the array on the 20 meter dish in Green Bank is the elements of the signal and noise correlation matrices. Tables 4.5 and 4.2 describe the parameters of the experiment and the model respectively.

The signal correlation matrix is approximated by $\mathbf{R}_s = \mathbf{R}_{on} - \mathbf{R}_{off}$, where $\mathbf{R}_{on}$ is the correlation matrix obtained when the reflector was pointed on source and $\mathbf{R}_{off}$ is the correlation matrix obtained when the reflector was off source. The noise correlation matrix is $\mathbf{R}_n = \mathbf{R}_{off}$. Figures 4.13–4.15 show the magnitudes of the elements of the signal and noise correlation matrices for the models and the experiment. The diagonal elements of the signal and noise correlation matrices are shown in Figure 4.16.

[2]Values in parenthesis are assumed as described in the text.

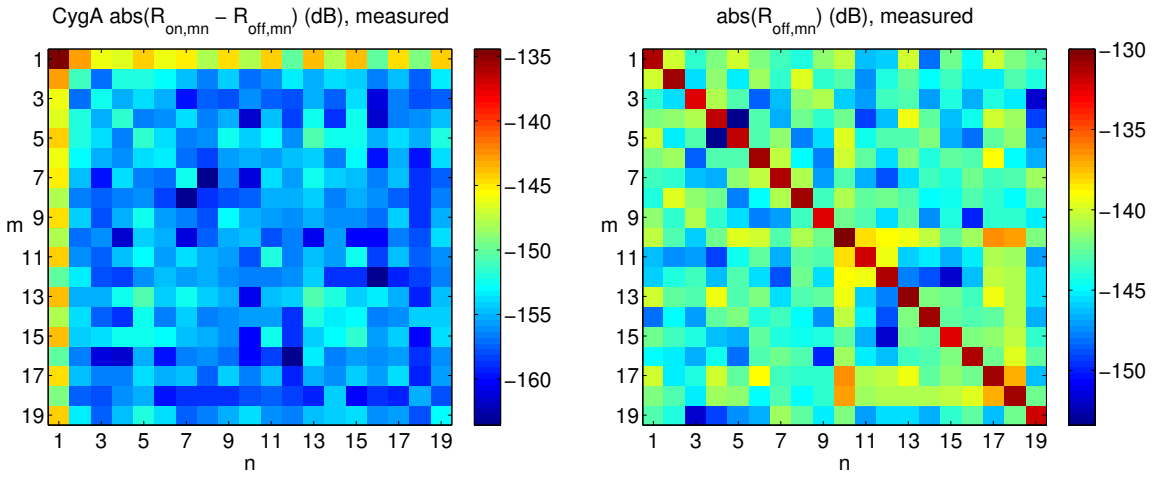

Figure 4.13: Magnitude of the elements of the signal and noise correlation matrices using experimental data, see Table 4.5 for a description of parameters related to these plots.

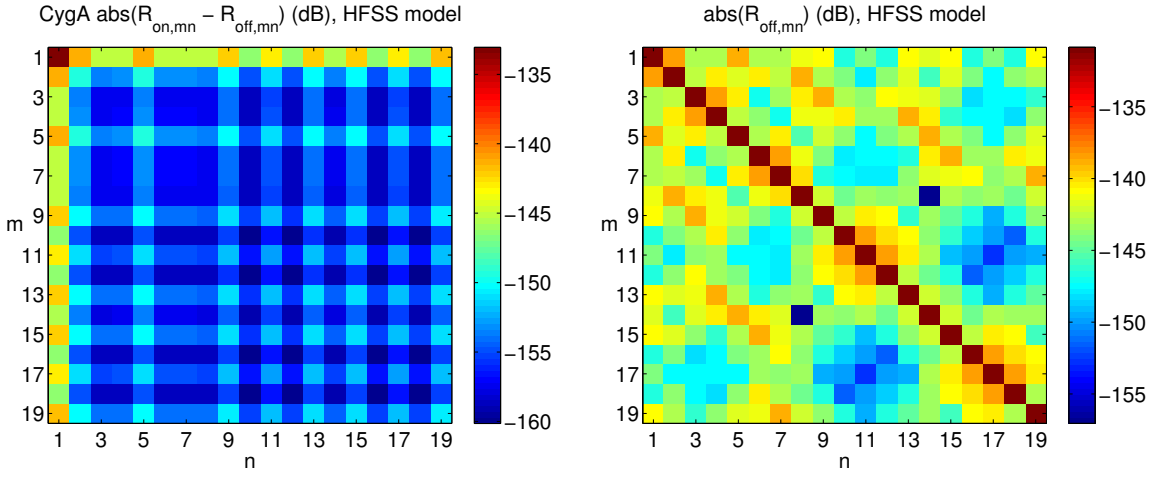

Figure 4.14: Magnitude of the elements of the signal and noise correlation matrices using the HFSS array model, see Table 4.2 for a description of parameters related to these plots.

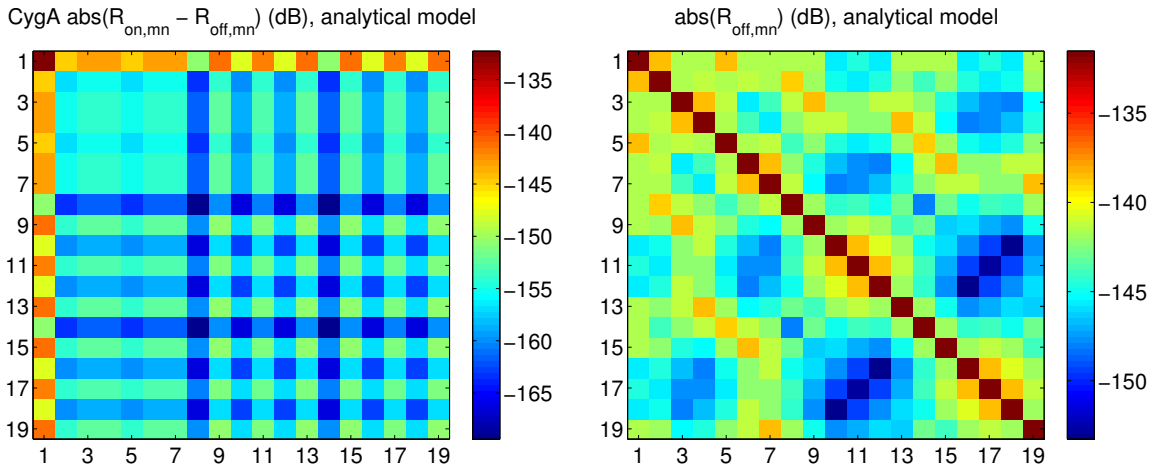

Figure 4.15: Magnitude of the elements of the signal and noise correlation matrices using the analytical array model, see Table 4.2 for a description of parameters related to these plots.

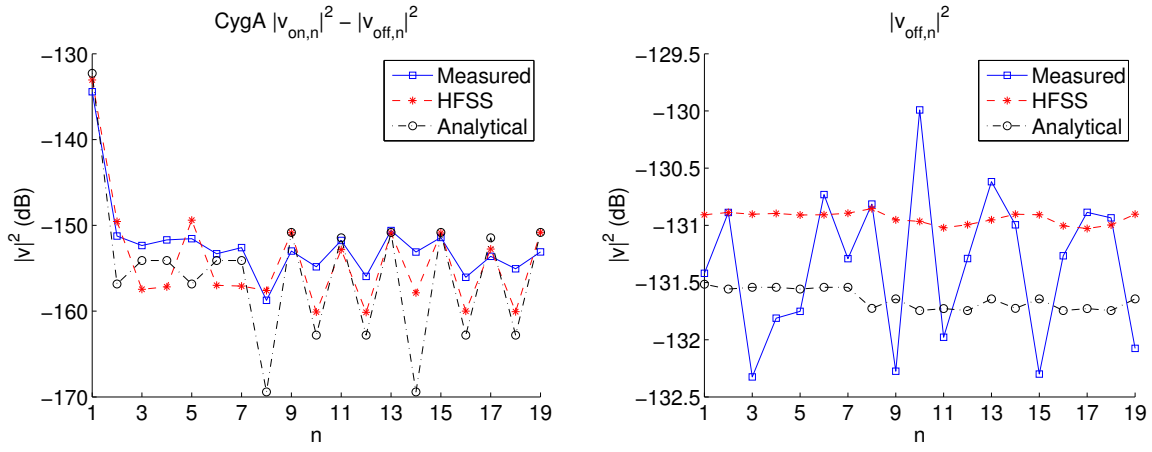

Figure 4.16: Magnitude of the diagonal elements of the signal and noise correlation matrices using experimental data and the HFSS and analytical models. See Tables 4.5 and 4.2 for a description of parameters related to these plots.

Table 4.5: Parameters of the experiment related to Figures 4.13–4.15.

Signal of interest	CygnusA (CygA)
Frequency	1600 MHz
F^{sig}	1380 Janskys
$F^{sig,p}$	690 Janskys
filename	/Nov02_2007/PassiveTests_2Nov07/corrBin/... CygA_10secOn_10secOff_corr.bin
Reflector diameter	20 meters
f/D	0.43
B_n	387.53 kHz

There are strong similarities in the correlation matrix structure of the two models, as seen in Figures 4.14 and 4.15. Both the models and the experimental data show that the center element receives much more signal than any other element when the reflector is steered on source, which is to be expected since the center element is located at the focal point of the reflector. The models and the experimental data also have noise correlation matrices that are strongly diagonal, which is to be expected because both $\mathbf{R}_{sp}$ and $\mathbf{R}_{lna}$ are strongly diagonal.

The signal correlation matrix from the experiment does not exhibit the same structure in elements 2–19 as the models do, which is most likely due to variations in the physical dimensions of the actual elements, and in variations in the receiver components. The same can be said for the off-diagonal elements of the noise correlation matrix. The noise correlation matrix from the experimental data shows some visible correlation structure between elements 10, 17, and 18. This could be caused by a signal in the sidelobes of those element's receive patterns.

4.5 Error Budget

This section discusses possible causes of the discrepancies between the measured and modeled figures of merit presented in Table 4.4. The results are compiled in the form of an error budget in Table 4.7. For simplicity only the difference between the experimental and the HFSS results using the maximum SNR beamformer will be studied. There is a -1.44 dB difference between the experimental A_e/T_{sys}

(1.289 m^2/K) and the A_e/T_{sys} obtained with the HFSS model (1.796 m^2/K). Each of the following paragraphs describes a possible cause of error between the measured and modeled results.

4.5.1 Coupling Increase

One difference between the model and the physical 19 element array is that the actual amount of coupling appears to be larger for some elements, see Figure 4.3. To determine the effect of more coupling in the array the off diagonal elements of the scattering matrix obtained with HFSS were multiplied by a scale factor and A_e/T_{sys} was recalculated. The difference in A_e/T_{sys} for three scale factors is shown in Table 4.6.

Table 4.6: Possible error caused by an increase in coupling

Scale Factor	Change in A_e/T_{sys} (dB)
1.05	-0.036
1.10	-0.071
1.20	-0.138

4.5.2 Self Impedance Difference

Another difference that is related to the impedance matrix of the array is the difference in self impedances of the elements, Figure 4.2 shows this difference. To account for the difference $7 + j10$ ohms were added to the diagonal terms of $\mathbf{Z}_A$. This created a -0.012 dB change in A_e/T_{sys}.

4.5.3 Sky Temperature

The model does not take into account the increase in system temperature due to thermal noise from the sky, if we assume that the brightness temperature of the sky is 3 K at L band frequencies, then the increase in system temperature is roughly 3 K. This changes the modeled A_e/T_{sys} by -0.071 dB.

4.5.4 Receiver Noise

There is some uncertainty in the noise parameters of the LNAs since none of the LNAs used in the experiment were characterized. The noise temperatures of the individual receivers, including the LNAs, were measured. The noise temperatures varied from 108 K to 162 K, with an average of 124 K. These are higher than would be expected given the noise parameters of two similar LNAs whose noise parameters were measured, see Table 4.3. Using the measured noise temperatures as the minimum noise temperatures of the LNAs, produced a -0.947 dB change in A_e/T_{sys}.

4.5.5 Reflector Model

There are also several aspects of the 20 meter reflector that are not included in the model, including diffraction and blockage caused by the feed and the support struts, edge diffraction, and surface inaccuracies. To estimate the error caused by these approximations in the reflector model the aperture efficiency was calculated using an idealized single feed with the modeled reflector. This aperture efficiency is then compared to the measured aperture efficiency of the 20 meter reflector at Green Bank when used with a single feed [32]. The measurements, taken over a bandwidth of 2.2 to 2.4 GHz, produced an aperture efficiency of 58 to 61%. The idealized feed is modeled as an antenna that produces a far field pattern that is proportional to

$$\overline{E} = \hat{\theta}\cos(\theta)^q \sin(\phi) + \hat{\phi}\cos(\theta)^q \cos(\phi). \tag{4.7}$$

Where q is chosen so that there is a -10 dB taper in the received power pattern along the reflector rim. Using this idealized feed the modeled aperture efficiency was 81.5%. Using a -14 dB taper instead produced an aperture efficiency of 76.6%. The difference in modeled A_e/T_{sys} due to this difference in aperture efficiency using the single feed is -1.258 dB for the -10 dB taper and -0.989 dB for the -14 dB taper. It is a first order approximation to consider all of this being due to differences between the modeled reflector and the actual reflector since the modeled feed may differ from the actual feed also.

4.5.6 Individual Element Patterns

Another possible difference between the physical array and the modeled array that could cause a change in A_e/T_{sys} is the individual element patterns. Even though this is not considered here, it is something that may need to be considered in future work.

4.5.7 Error Budget Summary

Table 4.7 summarizes the possible contributions of error between the experimental and modeled A_e/T_{sys} for the maximum SNR beamformer.

Table 4.7: Error budget

Source of error	Change in modeled A_e/T_{sys} (dB)
Coupling increase (1.1)	-0.071
Self impedance difference	-0.012
Sky temperature	-0.071
Receiver noise	-0.947
Reflector model	-0.989
Individual element patterns	NA
Total	-2.090
Actual	-1.44

It would appear that most of the error is from either differences between the modeled and actual LNAs and receiver chains or from aspects of the reflector that are not included in the model. The other sources of error appear to cause relatively insignificant changes in the overall system performance.

Chapter 5

Conclusion and Future Work

A promising level of agreement between the electromagnetic and signal processing models and the prototype 19 element phased array feed has been achieved. The models utilize signal and noise correlation matrices along with well known antenna parameters such as signal to noise ratio, efficiency, equivalent noise temperature, and available power to characterize the array.

Modeling the array feed using numerical methods, such as the finite element method, increases the accuracy of the models when compared to the analytical model. In spite of this, the analytical model provides valuable insight to many aspects of the phased array feed, and is much simpler to use.

5.1 Future Work

An even greater level of agreement between the PAF models and experimental data is needed in the future. Future work will be centered on obtaining additional measurements which provide more insight to the characteristics of PAFs.

As mentioned in Section 4.3 and Section 4.5 there is a level of uncertainty in obtaining the aperture efficiency and the system temperature from the experimental data because $\mathbf{R}_{te}$ is not known. Making time consuming S-parameter measurements in an anechoic chamber is one potential method for obtaining this, however, other methods may be available that have significant advantages over S-parameter measurements and produce similar results.

An increase in receiver noise temperature due to an increase in mutual coupling has been shown in the models, but has yet to be verified experimentally. This will be an important milestone in verification of coupled array and receiver noise models.

Hardware improvements in the array will also likely be a significant portion of the future work. Dual polarized antenna elements that operate over an increased bandwidth are likely be explored and implemented. A larger array with more elements will also likely be investigated and implemented. These improvements will greatly increase the complexity of both the models and the experimental data, but they will also bring the goal of creating a scientifically worthy radio telescope based on PAF technology several steps closer.

Bibliography

[1] J. D. Kraus, *Radio Astronomy*, 2nd ed. Powell, Ohio: Cygnus-Quasar Books, 1986. 1, 24

[2] K. Rohlfs and T. L. Wilson, *Tools of Radio Astronomy*, 4th ed. Berlin, Germany: Springer, 2004. 1

[3] M. A. B. Terada and W. L. Stutzman, "Computer-aided design of reflector antennas: The Green Bank radio telescope," *IEEE Trans. Microw. Theory Tech.*, vol. 46, no. 3, pp. 250–253, March 1998. 1

[4] P. A. Castleberg and K. M. Xilouris, "The Arecibo observatory," *IEEE Potentials*, vol. 16, no. 3, pp. 33–35,38–39, August–September 1997. 1

[5] P. J. Napier, A. R. Thompson, and R. D. Ekers, "The very large array: Design and performance of a modern synthesis radio telescope," *Proceedings of the IEEE*, vol. 71, no. 11, pp. 1295–1320, November 1983. 1

[6] International SKA Steering Commitee, "SKA project home page," 2008, see http://www.skatelescope.org/. 1

[7] L. Belostotski and J. W. Haslett, "Sub-0.2 dB noise figure wideband room-temperature CMOS LNA with non-50Ω signal-source impedance," *IEEE J. Solid-State Circuits*, vol. 42, no. 11, pp. 2492–2502, November 2007. 1

[8] G. L. James, "Wideband feed systems for radio telescopes," in *IEEE MTT-S International Microwave Symposium Digest*, vol. 3, June 1992, pp. 1361–1363. 1

[9] L. Staveley-Smith, W. E. Wilson, T. S. Bird, M. J. Disney, R. D. Ekers, K. C. Freeman, R. F. Haynes, M. W. Sinclair, R. A. Vaile, R. L. Webster, and A. E. Wright, "The Parkes 21-cm multibeam receiver," *Publications of the Astronomical Society of Australia, PASA*, vol. 13, no. 3, pp. 243–248, 1996. 2

[10] A. W. Rudge and M. J. Withers, "Beam-scanning primary feed for parabolic reflectors," *Electronics Letters*, vol. 5, no. 3, pp. 39–41, February 1969. 2

[11] P. Shelton, "Multiple-feed systems for objectives," *IEEE Trans. Antennas Propag.*, vol. 13, no. 6, pp. 992–994, November 1965. 2

[12] K. F. Warnick and M. A. Jensen, "Effects of mutual coupling on interference mitigation with a focal plane array," *IEEE Trans. Antennas Propag.*, vol. 53, no. 8, pp. 2490–2498, August 2005. 2, 3

[13] ——, "Optimal noise matching for mutually coupled arrays," *IEEE Trans. Antennas Propag.*, vol. 55, no. 6, pp. 1726–1731, June 2007. 2, 3

[14] R. Maaskant and E. Woestenburg, "Applying the active antenna impedance to achieve noise match in receiving array antennas," in *IEEE Antennas Propag. International Symposium*, June 2007, pp. 5889–5892. 2, 3, 21

[15] J. R. Fisher and R. F. Bradley, "Full sampling array feeds for radio telescopes," in *Proceedings of SPIE, Radio Telescopes*, vol. 4015, 2000, pp. 308–318. 2

[16] S. G. Hay, J. D. O'Sullivan, J. S. Kot, C. Granet, A. Grancea, A. R. Forsyth, and D. H. Hayman, "Focal plane array development for ASKAP (Australian SKA pathfinder)," in *European conference on antennas and propagation, EuCAP*, Edinburgh, UK, November 2007, pp. 1–5. 2

[17] R. Maaskant, M. V. Ivashina, R. Mittra, W. Yu, and N.-T. Huang, "Parallel FDTD modeling of a focal plane array with vivaldi elements on the highly parallel LOFAR BlueGene/L supercomputer," in *IEEE Antennas Propag. Society International Symposium*, June 2006, pp. 3861–3864. 2

[18] B. Veidt and P. Dewdney, "A phased-array feed demonstrator for radio telescopes," in *Proc. URSI General Assembly*, 2005. 2

[19] C. K. Hansen, K. F. Warnick, B. D. Jeffs, J. R. Fisher, and R. Bradley, "Interference mitigation using a focal plane array," *Radio Science*, vol. 40, no. 5, 2005, RS5S16, doi:10.1029/2004RS003138. 2, 3, 49

[20] J. R. Nagel, K. F. Warnick, B. D. Jeffs, J. R. Fisher, and R. Bradley, "Experimental verifcation of radio frequency interference mitigation with a focal plane array," *Radio Science*, vol. 42, 2007, RS6013, doi:10.1029/2007RS003630. 2

[21] M. V. Ivashina, E. E. M. Woestenburg, and E. A. Redkina, "Effects of the element separation on the noise performance of receiving antenna arrays," in *International Conference on Antenna Theory and Techniques*, Sevastopol, Ukraine, September 2007, pp. 82–86. 3

[22] K. F. Warnick and B. D. Jeffs, "Gain and aperture efficiency for a reflector antenna with an array feed," *IEEE Antennas Wireless Propag. Lett.*, vol. 5, no. 1, pp. 499–502, December 2006. 8, 14, 22

[23] ——, "Beam efficiencies and system temperature for a focal plane array," Technical Report, Brigham Young University, Provo, UT, November 2007, https://dspace.byu.edu/handle/1877/588. 8, 20, 21

[24] K. F. Warnick, P. Russer, and L. Belostotski, "Minimizing the noise penalty due to mutual coupling for a receiving array," Technical Report, Brigham Young University, Provo, UT, March 2008, https://dspace.byu.edu/handle/1877/621. 8, 21

[25] C. A. Balanis, *Antenna Theory*, 3rd ed. Hoboken, New Jersey: John Wiley & Sons, Inc., 2005. 8, 21, 31

[26] W. A. Imbriale, P. G. Ingerson, and W. C. Wong, "Large lateral feed displacements in a parabolic reflector," *IEEE Trans. Antennas Propag.*, vol. 22, no. 6, pp. 742–745, November 1974. 11

[27] C. Scott, *Modern methods of reflector antenna analysis and design.* Norwood, MA: Artech House, 1990. 12

[28] R. Q. Twiss, "Nyquist's and Thévenin's theorems generalized for nonreciprocal linear networks," *Journal of Applied Physics*, vol. 26, pp. 599–602, May 1955. 15

[29] "IEEE standard definitions of terms for antennas," IEEE Std 145-1993. 21

[30] J. R. Nagel, "A prototype platform for array feed development," Master's thesis, Brigham Young University, Provo, UT, December 2006. 33, 35, 37

[31] J. C. Tippet and R. A. Speciale, "A rigorous technique for measuring the scattering matrix of a multiport device with a 2-port network analyzer," *IEEE Trans. Microw. Theory Tech.*, vol. MTT-30, no. 5, pp. 661–666, May 1982. 34

[32] National Radio Astronomy Observatory (NRAO), "Information about the Green Bank 20-meter telescope," June 2008, see http://www.gb.nrao.edu/fgdocs/20m/GB20m.html. 55

APPENDIX

Appendix A

Coordinate System

Separate coordinate systems are used in this thesis when discussing a bare array with no reflector antenna and an array mounted on or near the focal plane of a reflector antenna. The coordinate system used in the former case (no reflector) is shown in Figure A.1. The ground plane lies on the x-y plane and the origin is located at the center of the ground plane. The coordinate system used in the latter case (with reflector) is shown in Figure A.2. The origin is located at the focal point of the parabolic reflector.

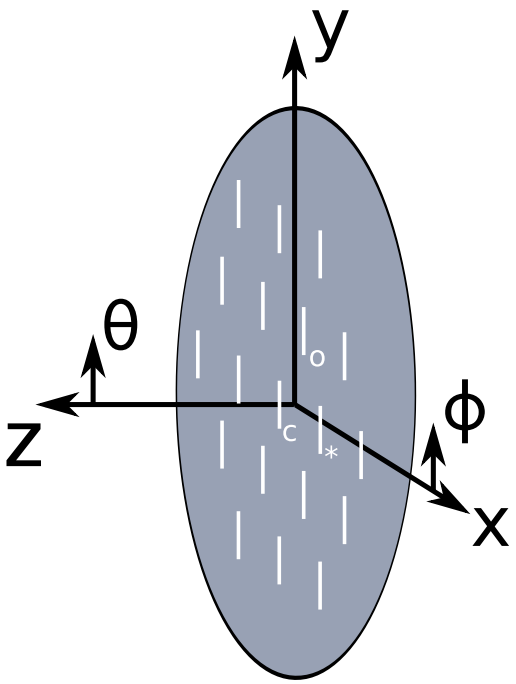

Figure A.1: Coordinate system used when discussing the bare array without the reflector antenna. The identifiers (c), (*), and (o) next to the dipoles are used to determine the orientation of the array when placed on the reflector, see Figure A.2. The ground plane lies on the x-y plane and the origin is located at the center of the ground plane. This drawing is not to scale.

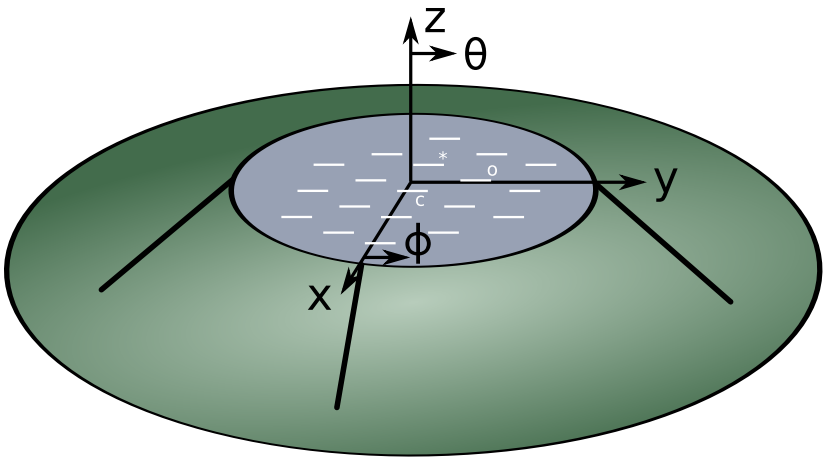

Figure A.2: Coordinate system used when discussing the array mounted on or near the focal plane of a reflector antenna. The identifiers (c), (*), and (o) next to the dipoles are used to determine the orientation of the array when placed on the reflector compared to the orientation of the bare array, see Figure A.1. The ground plane is depicted as being transparent so that the dipoles are visible. The origin is the focal point of the reflector. This drawing is not to scale.

Appendix B

Code Description

This appendix describes how to use the modeling codes that were used to obtain the overlap matrix, $\mathbf{A}$, and the array response matrix, $\mathbf{B}_{co}$, from the stored HFSS electric fields and using the analytical model. The modeling codes were written using MATLAB (The MathWorks). The codes consist of six functions along with a top level script that uses the functions. The hierarchy of the functions is given along with a description of each function, including the input and output parameters. The most recent versions of the codes are found on the wiki at https://www.et.byu.edu/groups/radioastron/dokuwiki/doku.php.

Figure B.1 shows the hierarchy of the modeling codes. Each block represents a MATLAB m-file (function or script). The function *bare_array_response* is the lowest level function and it is used by *overlap_matrix*, *reflector_response*, and *reflector_response2*. The function *array_element_response* calls either *reflector_response* or *reflector_response2* depending on the method desired to implement the physical optics approximation, see Section 2.1.1. Many of the figures generated in this thesis used different top level codes, usually a generic top level code was modified to suit the needs of various simulations.

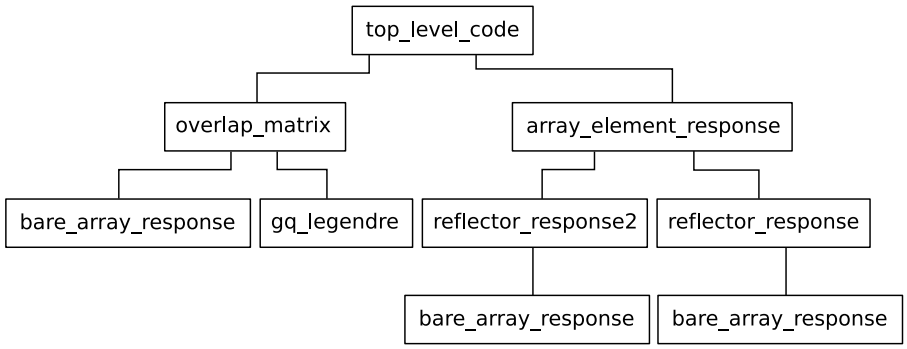

Figure B.1: Modeling code hierarchy. Each block represents a MATLAB m-file (function or script). The function *array_element_response* calls either *reflector_response* or *reflector_response2* depending on the method desired to implement the physical optics approximation, see Section 2.1.1. Many of the figures generated in this thesis used different top level codes, usually a generic top level code was modified to suit the needs of various simulations.

B.1 Function: bare_array_response

This function is used to obtain the far electric field of the elements of an array with no reflector, $\overline{E}_m^i(\bar{r})$ for $m = \{1, 2, \ldots, N\}$. The coordinate system assumed by this function is shown in Figure A.1. The input arguments and outputs of this function are described in the following sections.

B.1.1 Input Arguments

freq The frequency at which to compute the electric fields. Units: Hertz. Dimensions: scalar.

r The (x,y,z) coordinates of the dipoles relative to the center of the ground plane if a ground plane exists or relative to the center of the array if a ground plane does not exist. This input has no effect if opt{1} = 3. Units: meters. Dimensions: N x 3 matrix.

theta_far Far field elevation angles at which to compute the electric fields. The angles must lie either in the range $[0, \pi]$ or $[-\pi, 0]$. Units: radians. Dimensions: N_θ x 1 vector, where N_θ is arbitrary.

phi_far Far field azimuth angles at which to compute the electric fields. The angles must lie either in the range $[0, 2\pi]$ or $[-\pi, \pi]$. Units: radians. Dimensions: N_ϕ x 1 vector where N_ϕ is arbitrary.

gp Ground plane flag. This flag has no effect if opt{1} = 3. Units: none. Dimensions: scalar.

- **1** Include the effects of an infinite ground plane using image theory.
- **0** Do not include a ground plane.

gpo Ground plane offset. The (x,y,z) coordinates of the center of the ground plane relative to the origin. Units: meters. Dimensions: 1 x 3 vector.

opt Antenna options. Units: none. Dimensions: A scalar, a vector, or a cell array.

- **Hertzian dipole** Set opt(1) = 0 and opt(2) = kl, where k is the free space wavenumber corresponding to the input argument freq and l is the full length of the dipole. This function assumes that the dipoles are oriented in the $\hat{y}$ direction.
- **Isotropic radiator** Set opt(1) = 1.
- **Linear dipole** This is the option used for the analytical model mentioned in this thesis. Set opt(1) = 2 and opt(2) = kl, where k is the free space wavenumber corresponding to the input argument freq and l is the full length of the dipole. This function assumes that the dipoles are oriented in the $\hat{y}$ direction.

HFSS Set opt{1} = 3. Also, opt{2} is a string containing the filename and path of the .mat file containing the HFSS electric fields and opt{3} is a string containing the filename and path of the .mat file containing the angles at which the HFSS electric fields are defined.

single A flag used to indicate whether the fields from all the elements or a single element in the array are calcuated. Units: none. Dimensions: scalar.

0 The electric fields from all the elements are calculated.

m The electric field from the mth element is calculated.

EP_HP A flag used to indicate whether or not the ϕ dependence is removed. This is useful for finding E_P and H_P in Equation (2.15). The function *reflector_response* uses this option. This option is not compatible with opt{1} = 3. Units: none. Dimensions: scalar.

1 Compute the elctric field with the ϕ dependence removed.

0 Compute the electric field as normal.

B.1.2 Output

E_far Far electric field of the elements of an array. The e^{-jkr}/r term is not included. The input current, I_0, is assumed to be unity. Units: Volts. Dimensions: N x N_θ x N_ϕ x 2 array, where N_θ is the length of the input vector theta_far and N_ϕ is the length of the input vector phi_far. E_far(:,:,:,1) is the θ component of the electric field and E_far(:,:,:,2) is the ϕ component.

B.2 Function: reflector_response2

This function is used to obtain the far electric field of the elements of an array near the focal plane of a parabolic reflector, $\overline{E}_m^r(\bar{r})$ for $m = \{1, 2, \ldots, N\}$, see Equation (2.13). The physical optics approximation is used. The coordinate system assumed by this function is shown in Figure A.2. The input arguments and outputs of this function are described in the following sections.

B.2.1 Input Arguments

freq The frequency at which to compute the electric fields. Units: Hertz. Dimensions: scalar.

D Diameter of the reflector. Units: meters. Dimensions: scalar.

foD Focal length of the reflector divided by D. Units: none. Dimensions: scalar.

r This input is passed directly on to *bare_array_response*.

theta_far Far field elevation angles at which to compute the electric fields. The angles must lie either in the range $[0, \pi]$ or $[-\pi, 0]$. Units: radians. Dimensions: N_θ x 1 vector, where N_θ is arbitrary.

phi_far Far field azimuth angles at which to compute the electric fields. The angles must lie either in the range $[0, 2\pi]$ or $[-\pi, \pi]$. Units: radians. Dimensions: N_ϕ x 1 vector where N_ϕ is arbitrary.

gp This input is passed directly on to *bare_array_response*.

gpo Ground plane offset. The (x,y,z) coordinates of the center of the ground plane relative to the origin of the reflector's coordinate system (the focal point). Units: meters. Dimensions: 1 x 3 vector.

opt This input is passed directly on to *bare_array_response*.

single The element number to calculate the electric field for (m). Units: none. Dimensions: scalar.

B.2.2 Output

E_far Far electric field of a single element in an array located near the focal plane of a parabolic reflector. The e^{-jkr}/r term is not included. The input current, I_0, is assumed to be unity. Units: Volts. Dimensions: N_θ x N_ϕ x 3 array, where N_θ is the length of the input vector theta_far and N_ϕ is the length of the input vector phi_far. E_far(:,:,1), E_far(:,:,2), and E_far(:,:,3) are the x, y, and z components of the electric field respectively

B.3 Function: reflector_response

This function is used to obtain the far electric field of the elements of an array near the focal plane of a parabolic reflector, $\overline{E}_m^r(\bar{r})$ for $m = \{1, 2, \ldots, N\}$, see Equation (2.13). The one dimensional physical optics approximation is used, as described in Section 2.1.1. The coordinate system assumed by this function is shown in Figure A.2. The input arguments and outputs of this function are described in the following sections.

B.3.1 Input Arguments

freq The frequency at which to compute the electric fields. Units: Hertz. Dimensions: scalar.

D Diameter of the reflector. Units: meters. Dimensions: scalar.

foD Focal length of the reflector divided by D. Units: none. Dimensions: scalar.

offset The (x,y,z) coordinates of the mth element relative to the origin of the reflector's coordinate system (the focal point).

theta_far Far field elevation angles at which to compute the electric fields. The angles must lie either in the range $[0, \pi]$ or $[-\pi, 0]$. Units: radians. Dimensions: N_θ x 1 vector, where N_θ is arbitrary.

phi_far Far field azimuth angles at which to compute the electric fields. The angles must lie either in the range $[0, 2\pi]$ or $[-\pi, \pi]$. Units: radians. Dimensions: N_ϕ x 1 vector where N_ϕ is arbitrary.

gp This input is passed directly on to *bare_array_response*.

gpo Ground plane offset. The (x,y,z) coordinates of the center of the ground plane relative to the origin of the reflector's coordinate system (the focal point). Units: meters. Dimensions: 1 x 3 vector.

opt This input is passed directly on to *bare_array_response*.

B.3.2 Output

E The y component of the far electric field of a single element in an array located near the focal plane of a parabolic reflector. The e^{-jkr}/r term is not included. The input current, I_0, is assumed to be unity. Units: Volts. Dimensions: N_θ x N_ϕ matrix, where N_θ is the length of the input vector theta_far and N_ϕ is the length of the input vector phi_far.

B.4 Function: array_element_response

This function is used to obtain the array response matrix, $\mathbf{B}_{co}$ or $\mathbf{B}_{cross}$, from the electric fields obtained with either *reflector_response* or *reflector_response2*. The coordinate system assumed by this function is shown in Figure A.2. The input arguments and outputs of this function are described in the following sections.

B.4.1 Input Arguments

freq The frequency at which to compute the electric fields. Units: Hertz. Dimensions: scalar.

r The (x,y,z) coordinates of the dipoles relative to the center of the ground plane if a ground plane exists or relative to the center of the array if a ground plane does not exist. Units: meters. This input has no effect if opt{1} = 3. Dimensions: N x 3 matrix.

gpo This input is passed directly on to *reflector_response* and *reflector_response2*.

theta_far This input is passed directly on to *reflector_response* and *reflector_response2*.

phi_far This input is passed directly on to *reflector_response* and *reflector_response2*.

D This input is passed directly on to *reflector_response* and *reflector_response2*.

foD This input is passed directly on to *reflector_response* and *reflector_response2*.

gp This input is passed directly on to *reflector_response* and *reflector_response2*.

pol A string describing the polarization of the fields to use in calculating **B**. Units: none. Dimensions: character.

'y' Calculate $\mathbf{B}_{co}$. The dipoles are assumed to be oriented in the $\hat{y}$ direction.

'x' Calculate the x component of $\mathbf{B}_{cross}$. This option is not compatible with ver = 1.

ver A flag used to determine which physical optics code to use. Units: none. Dimensions: scalar.

1 Use the one dimensional physical optics code, *reflector_response*.

2 Use the two dimensional physical optics code, *reflector_response2*.

opt This input is passed directly on to *reflector_response* and *reflector_response2*.

B.4.2 Outputs

Ep The co or cross polarized component of the far electric field for the elements in an array located near the focal plane of a parabolic reflector. The e^{-jkr}/r term is not included. The input current, I_0, is assumed to be unity. Units: Volts. Dimensions: N x N_θ x N_ϕ matrix, where N_θ is the length of the input vector theta_far and N_ϕ is the length of the input vector phi_far.

Bp The co or cross polarized component of the array response matrix for an array located near the focal plane of a parabolic reflector. The $1/r^2$ term is not included. The input current, I_0, is assumed to be unity. Units: Watts. Dimensions: N x N x N_θ x N_ϕ array, where N_θ is the length of the input vector theta_far and N_ϕ is the length of the input vector phi_far.

B.5 Function: overlap_matrix

This function is used to obtain the overlap matrix, **A**, and the spillover matrix, $\mathbf{A}_{sp}$ for an array of antennas located near the focal plane of a reflector antenna that is pointed towards zenith. This function uses a Gaussian-Legendre quadrature rule to integrate the bare array electric fields in θ and a midpoint quadrature rule to integrate the fields in ϕ.

B.5.1 Input Arguments

r The (x,y,z) coordinates of the dipoles relative to the center of the ground plane if a ground plane exists or relative to the center of the array if a ground plane does not exist. Units: meters. This input has no effect if opt{1} = 3. Dimensions: N x 3 matrix.

freq The frequency at which to compute the electric fields. Units: Hertz. Dimensions: scalar.

theta_reflector_rim The angle extending from the center of the reflector to the rim. Set theta_reflector_rim = [ ] if $\mathbf{A}_{sp}$ is not needed. Units: radians. Dimensions: scalar.

gp This input is passed directly on to *bare_array_response*.

opt This input is passed directly on to *bare_array_response*.

B.5.2 Outputs

A_total The overlap matrix, **A**, for the array and frequency specified by the input arguments. Units: Watts. Dimensions: N x N.

A_spill The spillover matrix, $\mathbf{A}_{sp}$, for the array, theta_reflector_rim, and frequency specified by the input arguments. Units: Watts. Dimensions: N x N.

B.6 Function: gq_legendre

This function is used to obtain the weights and nodes of a Gaussian-Legendre quadrature rule.

B.6.1 Input Argument

N The number of weights and nodes to calculate.

B.6.2 Outputs

w The weights of the Gaussian-Legendre quadrature rule that correspond to the nodes, x. Units: none. Dimensions: 1 x N, where N is the input argument.

x The nodes of the Gaussian-Legendre quadrature rule, in descending order. Units: none. Dimensions: 1 x N, where N is the input argument.